Journal of Rock Mechanics and Geotechnical Engineering xxx (xxxx) 1–18

Contents lists available at ScienceDirect

Journal of Rock Mechanics and Geotechnical Engineering

journal homepage: www.elsevier.com/locate/JRMGE

Full Length Article

Thermo-hydro-mechanical dynamics of a rock slope: Integrated field and numerical analysis at the Požáry test site in the Czech Republic

Saeed Tourchi[a,*], Milad Jabbarzadeh[b], Arash Alimardani Lavasan[a], Hamed Sadeghi[b],
Ondřej Racek[c,d]

[a] Department of Engineering, Luxembourg University, Luxembourg, L-4365, Luxembourg
[b] Department of Civil Engineering, Sharif University of Technology, Tehran, 1458889694, Iran
[c] Institute of Rock Structure and Mechanics of the CAS, Prague, 18209, Czech Republic
[d] Charles University in Prague, Faculty of Science, Department of Physical Geography and Geoecology, Prague, Czech Republic

ARTICLE INFO

Article history:
Received 30 April 2024
Received in revised form 5 September 2024
Accepted 13 September 2024

Keywords:
Rock slope stability
Strain evolution
Fracture evolution
Thermo-hydro-mechanical (THM) coupling
Seasonal temperature changes

ABSTRACT

Understanding strain and fracture evolution in rock masses under climate change is crucial for slope stability. This study presents a fully coupled thermo-hydro-mechanical (THM) simulation of a rock slope at the Požáry test site in the Czech Republic, integrating field tests and laboratory analyses. The simulations used the exactly measured slope geometry and incorporated a pre-existing upper slope fracture. Key constitutive models for fluid and vapor flow, heat conduction, and porosity-dependent permeability were coupled with a viscoplastic damage model to capture the THM behavior of the rock slope. Laboratory tests on three rock samples (A, B, and C) with varying elastic moduli and porosities informed the material properties for three corresponding models. Simulation results showed greater thermal changes in the upper sections of the slope due to increased exposure to thermal effects. Model A, with the highest elastic modulus, exhibited lower initial strain changes, while Model C showed significant early strain variations. After 30 d, Model A experienced a sudden strain decrease due to thermal contraction-induced damage. The critical fractured zone (CFZ) analysis revealed that rock contraction under cooling led to an increase in pore water pressure, exacerbating the damage. Model B highlighted the impact of geometrical asymmetry on the propagation of the damaged zone. Over time, the thermal effects increased plastic deformation in Model A, while Model C remained elastic and exhibited no damage. These findings have significant implications for assessing rock slope stability, particularly in predicting failure zones due to permeability reduction and pore water pressure generation.

1. Introduction

Slope instability can be attributed to the failure of slope-forming materials, including rocks, soils, and artificial fills. These materials are subjected to gravitational forces and are influenced by a range of triggering factors, such as heavy rainfall, seismic activity, volcanic eruptions, and human alterations of the landscape (Varnes, 1958; Rodrıguez et al., 1999; Collins and Znidarcic, 2004). However, with the advent of climate change, temperature variations are becoming a cause of increasing concern. Temperature can induce time-dependent changes in rock properties and trigger thermal stresses that may contribute to the progressive weakening and eventual failure of rock cliffs (Alonso et al., 2016). Therefore, understanding these thermal effects is essential for predicting and mitigating the risk of slope instabilities.

Climate factors have brought about unprecedented shifts in environmental conditions, leading to alterations in temperature patterns and thermal regimes across diverse geological settings (Jabbarzadeh et al., 2024; Tourchi et al., 2024). Such changes have the potential to exert a profound effect on the mechanical properties of rocks, influencing their deformation characteristics and overall stability. Notably, studies by Wu et al. (2019) and Scaringi and Loche (2022) have emphasized the significance of considering climate-driven thermal variations in the assessment of slope stability. This emphasizes the need for a thorough understanding of the coupled processes that govern rock behavior under changing temperature regimes. The response of rock masses to temperature variations encompasses a range of complex phenomena, including thermal expansion and contraction, as well as associated volumetric changes (Gunzburger et al., 2005; Ghandilou et al., 2023). This phenomenon is exacerbated by the inhomogeneity of thermal expansion coefficients in different minerals, leading to microcracking and a gradual degradation of rock integrity (Zhang et al., 2001).

The thermo-mechanical behavior of rocks is influenced by several factors, including mineral composition, porosity, water content, and external loading conditions. When rocks are subjected to temperature gra-

---

[*] Corresponding author.
E-mail address: saeed.tourchi@uni.lu (S. Tourchi).

https://doi.org/10.1016/j.jrmge.2024.09.052
1674-7755/© 20XX

dients, thermal expansion, and contraction can induce internal stresses, which in turn lead to changes in their mechanical properties. Additionally, thermal cycling can cause fatigue and damage accumulation in rocks, which may ultimately affect their long-term stability. The experimental tests conducted by Sultan et al. (2002) revealed that at each temperature, the curves exhibited a volumetric yield point at a stress higher than 4 MPa, indicating a hardening phenomenon induced by heating. Furthermore, the stress value at which yield occurs decreases with increasing temperature. Tang et al. (2008) demonstrated that the volumetric thermal behavior of soils is significantly influenced by suction and pressure, with heating inducing expansion under certain conditions and contraction under others. The study revealed that heating clay at a low overconsolidation ratio (OCR) induced plastic contraction, while at a high OCR, heating induced expansion up to a certain temperature, followed by contraction. These findings indicate that OCR is not the sole controlling parameter of the thermal volumetric behavior of unsaturated soils, highlighting the complex interaction of factors influencing soil response to thermal changes. Furthermore, investigations by Chen et al. (2017) have elucidated the influence of temperature on the time-dependent response of granite rock. The findings of their study indicate that an increase in temperature within 200 °C may significantly weaken the rock and reduce the time to failure. Though such a high temperature is not relevant to climate change, it does demonstrate the potential for a less pronounced but still significant impact at lower temperature ranges. Similarly, Kumari et al. (2017) showed that elevated temperatures result in a reduction in the strength and elastic characteristics of granite, leading to a transition in failure behavior from brittle to quasi-brittle (Gomah et al., 2022; Wang et al., 2023, 2024).

In situ measurements play a crucial role in capturing the real-time response of rock slopes to influential factors, including temperature changes. The development of monitoring instruments, including strain gauges, extensometers, and inclinometers, has enabled researchers to quantify the deformation and strain patterns within rock masses subjected to thermal gradients. The work of Racek et al. (2023) exemplifies the use of in situ monitoring techniques to assess the influence of temperature variations on the stability of rock slopes, providing valuable insights into the temporal and spatial evolution of strain. Mufundirwa et al. (2011) used surface displacement sensors to monitor the deformation of a chert rock mass across fractures and to predict the deformations caused by thermal stresses using finite element analysis. Lan et al. (2021) used a ground-based synthetic aperture radar (GB-SAR) unit, displacement meter, and hygrothermographs to measure the cyclic expansion and contraction, moisture, and temperature variations of a loess slope. Moreover, Hugentobler et al. (2021) investigated and quantified the effects of thermo-hydro-mechanical (THM) rock slope processes that occur during deglaciation. They employed a subsurface monitoring system, including boreholes with sensors for measuring strain, temperature, and pore pressure, alongside high-resolution vertical FBG (fiber Bragg grating) strain sensors and in-place inclinometers for measuring horizontal deformation.

In addition to in situ measurements, numerical simulations have become an indispensable tool for analyzing the behavior of rock slopes under varying thermal conditions. Numerical approaches allow for the prediction of rock mass response to temperature changes, taking into account complex geometries, material properties, and boundary conditions. A study by Wu et al. (2019) demonstrated the efficacy of numerical simulations in understanding rock slope behavior. These simulations elucidate the mechanisms that govern temperature, pore water pressure, and plastic strain evolution under thermal, hydraulic, and mechanical loading. This approach offers a means of complementing and validating experimental observations. Marmoni et al. (2020) developed a thermo-mechanical numerical model to study the behavior of a rock wall in an abandoned quarry. The model was calibrated to match experimental temperature profiles and simulated heat propagation and irreversible effects. Additionally, a mechanical numerical analysis was performed using the finite difference method, considering stress–strain thermo-mechanical configuration. The study found that fluctuations in near-surface temperature can lead to long-term failure of rock blocks. Similarly, Thota and Vahedifard (2021) examined the impact of temperature on the stability of unsaturated intact slopes and developed an analytical framework to calculate the factor of safety under different thermal and seepage conditions. More recently, Tian et al. (2023) and Park et al. (2023) developed sufficiently accurate numerical models that consider the influence of temperature changes on slope stability.

From an energy point of view, the study by Xu et al. (2022) developed a thermal damage constitutive model for rock, incorporating energy principles, effective stress principles, and damage theory. The model effectively describes the full stress-strain curve of rock failure and reflects the state instability driven by energy dissipation. The study demonstrates that with increasing temperature, the peak stress, ultimate elastic energy, and dissipated energy at peak stress exhibit a logistic decline. This indicates that the mechanical properties of rock deteriorate with rising temperatures. Moreover, Zhang et al. (2023) conducted a comprehensive analysis of the energy dissipation of T-shaped fractured rock samples under varying loading rates. Initially, energy dissipation occurs primarily due to microfracture closure, with only a small portion converted to elastic energy. During the elastic stage, elastic energy dominates, whereas in the yield stage, the sample undergoes plastic deformation, intensifying damage and enhancing energy dissipation. In particular, as the loading rate rises, the elastic energy at the peak point increases, while dissipated energy decreases, reflecting the increased brittleness and reduced plastic deformation capability of the rock at higher strain rates. Furthermore, Sun et al. (2023) investigated the effects of cyclic loading and unloading on the energy dissipation mechanisms and mechanical properties of sandstone and granite. The findings indicate that cyclic loading-unloading paths lead to a hardening effect, where the strength of the rock under cyclic conditions exceeds that under uniaxial compression. The study reveals that under cyclic loading with large load cycles, the elastic energy dominates, illustrating the rocks' stronger elastic properties. Conversely, variable load cycles result in greater damage, with the damage energy becoming the dominant factor.

This study presents an integrated approach to investigating the dynamic interactions between temperature changes and subsequent strain evolution and volumetric behavior of a rock cliff. Resistivity strain gauges were utilized in various configurations to measure surface strain in natural conditions, with a focus on assessing the influence of temperature. The data collected from the Požáry test site in the Czech Republic via an Internet of Things (IoT) network database were analyzed to facilitate continuous monitoring of meteorological changes. Additionally, rock sampling was performed for laboratory tests to determine the rock's mechanical properties. The field and experimental data were then used in numerical simulations of the strain and temperature evolution within the rock slope, employing fully coupled THM modeling to investigate the response of the rock cliff to temperature changes.

2. Description of the in situ test site and monitoring program

A schematic representation of the rock cliff, subjected to variations in air temperature, is shown in Fig. 1. It is important to note that Fig. 1 is a schematic representation and is not drawn to scale. This rock slope is located at the Požáry test site in the Czech Republic, which is a recently established field laboratory. Instruments were installed to detect deformation in fractured rock masses. The Požáry test site, located in Central Bohemia (Fig. 2a), was previously a paving stone quarry and has since been transformed into a scientific research area equipped with a comprehensive set of instruments. A monitoring system includes a weather station that simultaneously monitors temperature changes, revealing thermal processes in the study area (Fig. 1). Temperature fluc-

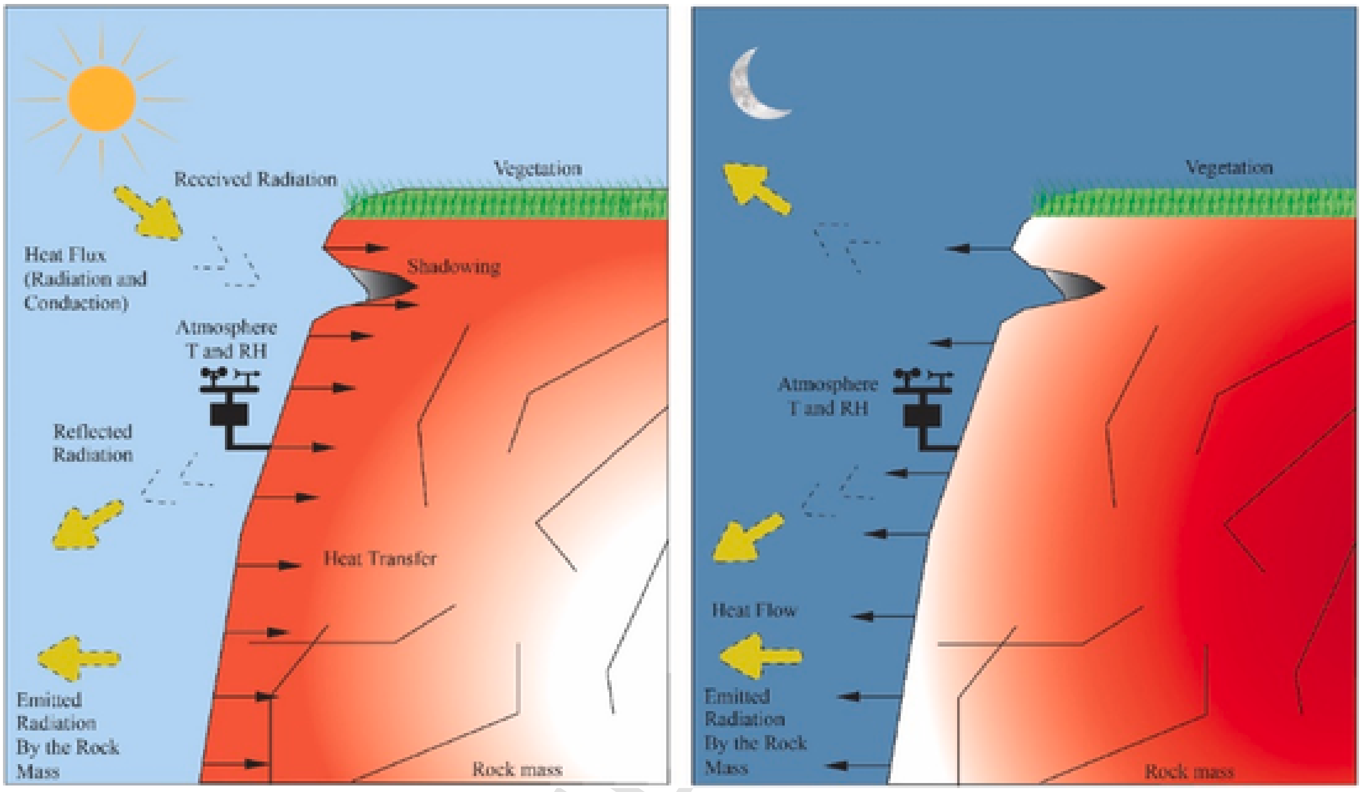

Fig. 1. Sketch of temperature processes depicting the instrumented rock cliff at the Požáry test site in the Czech Republic.

tuations cause thermal expansion or contraction in the rock mass, which can be monitored with the installed instruments.

The rock wall is relatively flat due to past tectonic and blasting activities, resulting in horizontal changes in the rock mass (Fig. 2b). The results of the tests on the rock samples indicated that the in situ conditions are complex, with the rock properties varying even within short distances. The locations of the sampling points for rock properties are marked by red dots and yellow circles in Fig. 2b.

Fig. 3 presents the experimental results for the rock samples labeled A, B, and C. The bulk, axial, and transverse strain behaviors for these samples obtained from uniaxial compression tests are shown in Fig. 3a–c, respectively, illustrating the distinct mechanical properties of each sample. Fig. 3d displays the rock samples collected from these three points. Based on these experimental results, the necessary elastic and material parameters for numerical simulation, including Young's modulus (E), Poisson's ratio (ν), grain density (ρ_s), and porosity (ϕ), were calculated and are summarized in Table 1. The additional parameters pertaining to the red dots were elucidated by Racek et al. (2023). The rock type is classified as either biotitic granodiorite or quartz diorite.

Fig. 2b and c illustrates the rock wall where a monitoring system, previously demonstrated to be operational in other contexts (Racek et al., 2023), was installed. A total of 11 strain gauges with different configurations were installed on the rock mass to monitor potential plastic strain over microfractures over two months, as shown in Fig. 2b and c. The sensors were installed using resin. They were affixed with a specialized HBM resin and then covered with a protective film, ensuring optimal adhesion to the rock surface. Induction crack meters were bolted to the rock mass surface. Fig. 2c depicts the strain gauges before applying protective aluminum foil. Evaluating strain in rock masses is important for slope stability studies. Strain is a function of stress, and stress can affect the mechanical properties of geomaterials, potentially leading to the destabilization of rock slopes. However, the measurement of in situ stress is challenging. Therefore, resistivity strain gauges were utilized in various configurations to measure surface strain in natural conditions, evaluating the impact of factors such as temperature and incoming solar radiation. In industrial applications, resistivity strain gauges are employed to measure strain, enabling the recording of even small changes in strain. Mathematical estimation of these factors, in conjunction with a data processing system, allows for the accurate processing of results from each configuration. The proposed strategy offers high theoretical accuracy that enables the detection of strain variations in field conditions. By adjusting for the influence of temperature, it is potentially possible to measure deformation trends more accurately while maintaining lower sensor costs. The data collected from the Požáry test site via an IoT network database were then analyzed, allowing continuous monitoring of meteorological changes.

Fig. 4 displays the strain and temperature variations recorded by the installed instruments on an intact rock surface as a reference for the behavior of the massive rock. These measurements include a period of 56 d, from October 16 to December 10, 2022. As shown in Fig. 4, the overall trend of the temperature exhibited a decline over the monitoring period of 56 d, resulting in a net thermal contraction of the rock surface (a reduction in strain). Fig. 5 illustrates the changes in microstrain and temperature over several consecutive days. In Fig. 5a, it is observed that as the time increases from 0 d to 0.7 d and 11.2 d–14.6 d, the microstrain also increases due to rock expansion. The difference between these two linear trends represents the rate of change in microstrain in response to temperature changes. In the initial stage of the measurements, the rate of microstrain variation is higher. For example, the rate of change is 12.858 from 0 d to 0.7 d and decreases to 10.692 from 11.2 d to 14.6 d. Conversely, when the air temperature decreases, the rock contracts and the microstrain decreases, as shown in Fig. 5b. The observed trends indicate that within specific timeframes of consecutive days, the relationship between microstrain and temperature is linear, but the long-term behavior is not linear. This is because the rate of

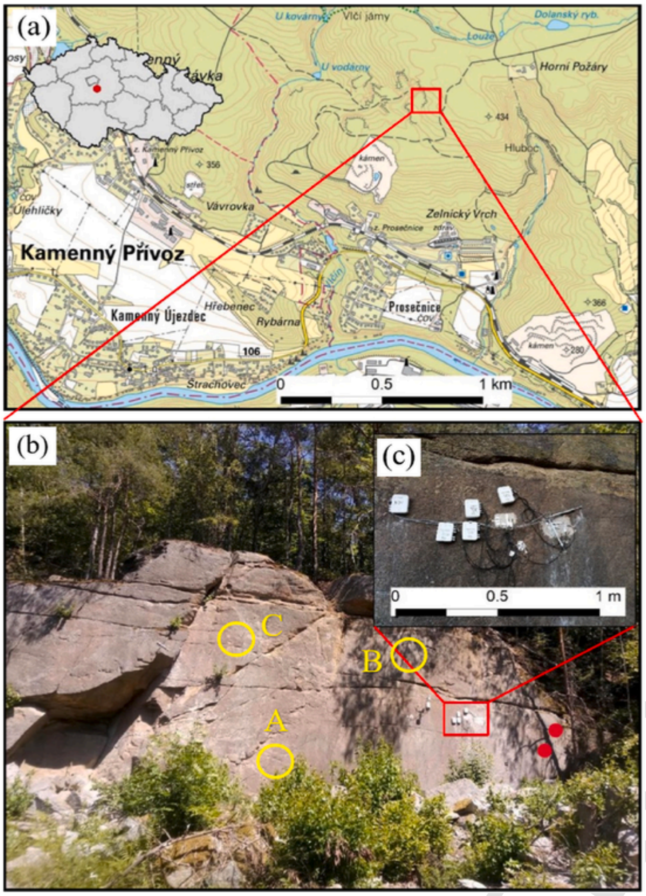

Fig. 2. Illustration of the Požáry test site: (a) Field laboratory location; (b) Overview of the instrumented rock wall; and (c) Close-up view showcasing the installed strain gauges and induction crack meters (Racek et al., 2023).

rock deformation decreases with an increase in temperature fluctuations.

Due to a lack of rock samples and monitoring instruments for the slope shown in Fig. 1, the parameters and measurements of the rock slope illustrated in Fig. 2 were used in numerical simulations. Consequently, data from in situ tests on three rock materials (A, B, and C) presented in Fig. 3 and Table 1 were utilized. Additionally, in situ measurements of strain changes caused by thermal processes, depicted in Fig. 1, were incorporated. Thereafter, numerical simulations (Models A, B, and C) corresponding to each rock material type were carried out to estimate the behavior of the rock slope.

3. Theoretical formulation

3.1. Coupled phenomena and THM formulation

The study of coupled THM phenomena plays a significant role in understanding the impact of climate-induced changes, particularly temperature fluctuations, on the deformation and stability of rock slopes. While the influence of temperature on evapotranspiration and hydrological balance is well-established, the direct coupling of thermo-mechanical processes is often overlooked (Scaringi and Loche, 2022). This oversight contrasts with the abundance of experimental evidence that demonstrates fully coupled THM behaviors in various geomaterials, even within temperature ranges that are commonly experienced at the ground surface or in the near subsurface. Temperature fluctuations may exert hydro-mechanical forces on slopes over short or long periods, and may change its stability condition.

In addition, the thermal volume changes of soil depend on its hydraulic conditions such as pore water pressure and permeability. Experimental studies generally conclude that the thermal volume change in a clay sample is influenced by factors such as OCR, pore water pressure, and confining pressure (Sultan et al., 2002; Tang et al., 2008). Therefore, this study focuses on a fully coupled THM analysis of a rock cliff undergoing temperature changes. The aim is to investigate its strain evolution, volume change behavior, and temperature distribution, comparing the results with existing in situ measurements.

The model's geometry was constructed using precise field measurements of the slope's surface. The horizontal side is extended to an appropriate length to avoid boundary effects while avoiding excessive computational intensity. The model's geometry, finite element mesh, and initial boundary conditions are illustrated in Fig. 6. The initial temperature of the entire domain was assumed to be equal to 12 °C (the initial value of the measured temperature variations), with a variable boundary condition on the left and top boundaries (Fig. 4). The study neglects plant coverage on the top boundary, assuming the same temperature variations for both boundaries. As a mechanical initial boundary condition, an initial stress of 10 kPa is assigned to the top boundary and the entire domain. Since water flux is not reported in field observations, the initial hydraulic flow rate is not assigned, and the rock medium is assumed to be saturated. Three models (Models A, B, and C) are presented to account for different rock material types (Table 1). The initial and boundary conditions remain the same for all models. The simulations include 56 d of THM analysis, with temperature changes occurring every 0.1 d, resulting in 560 temporal steps.

As shown in Fig. 6, the model was discretized by three lines, each representing a distinct section of the rock slope surface within the rock mass. The categorization into top, middle, and bottom lines was based on the geometric and boundary condition variations that each section experiences. Specifically, the top line is subjected to two boundary conditions pertaining to temperature variations, given its exposure to atmospheric conditions. The middle line is characterized by the presence of an initial fracture, which significantly influences its mechanical and thermal behavior. The bottom line features a flatter geometry and is exposed to air temperature gradients from a single direction. This categorization is based on the rationale that it is necessary to capture the distinct spatio-temporal behavior of the entire rock slope under varying conditions.

The coupled THM formulations employed in this study have been previously described by Olivella et al. (1994, 1996) and Gens and Olivella (2001), For the sake of brevity, a summary will be provided here. In the theoretical framework adopted for this study, a multiphase and multispecies methodology is employed. The phases are distinguished using subscripts (s: solid, l: liquid, g: gas), while the species are identified using superscripts (w: water, a: dry air). Consequently, the state variables (unknowns) encompass displacement, $\boldsymbol{u}$ (m), liquid pressure, P_{l} (MPa), and soil temperature, T (◦ C).

A general balance equation consists of three components: the temporal change of a property within the porous material, the divergence of the flux of the aforementioned property, and the rate of production/decay of the property:

$$\frac{\partial}{\partial t}(\rho \cdot \psi) + \nabla \cdot \left(j_{\psi}\right) - f^{\psi} = 0 \tag{1}$$

where ψ represents the property per unit mass, ρ is the density, j_{ψ} indicates the total mass flux of ψ, and f^{ψ} denotes the rate of production/decay of ψ per unit volume. Employing a compositional approach (Panday and Corapcioglu, 1989), the volumetric mass of a species in a phase (θ_{ψ}) is determined by the product of the mass fraction of that species (ω_{ψ}) and the bulk density of the phase (ρ).

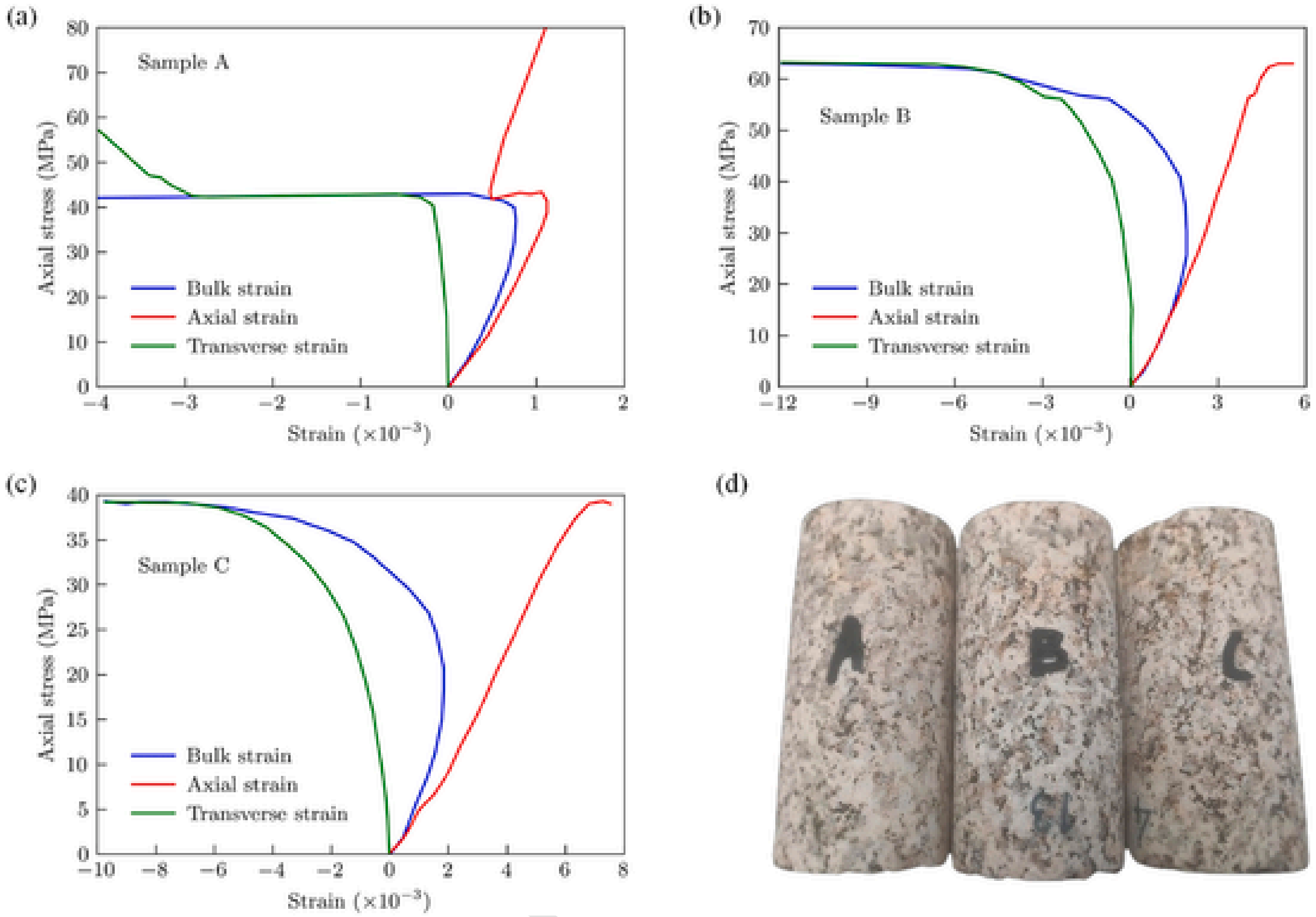

Fig. 3. Experimental results of stress–strain curves for (a) sample A, (b) sample B, (c) sample C, and (d) representation of rock samples collected from three points of the slope.

Table 1
Descriptive and mechanical properties of Požáry granodiorite.

Material	Young's modulus, E (MPa)	Poisson's ratio, ν	Grain density, ρ_s (kg/m^3)	Porosity, ϕ (%)
A	31,600	0.2	2667	0.9
B	15,800	0.13	2662	1.69
C	5600	0.06	2649	3.75

This general equation can be divided into three balance equations: the solid mass balance that determines the porosity changes over time, the water mass balance that incorporates both liquid and gas phases and determines liquid pressure changes over time, and the internal energy balance that determines temperature changes over time. Moreover, the momentum balance was considered as a stress equilibrium equation by neglecting inertial terms:

$$\nabla.\boldsymbol{\sigma} + \boldsymbol{b} = 0 \tag{2}$$

where $\boldsymbol{\sigma}$ is the total stress tensor, and $\boldsymbol{b}$ is the vector of body forces. Ultimately, strain evolution can be obtained by solving the momentum balance equation. The following section explains the constitutive equations of the model.

3.2. Thermal and hydraulic constitutive equations

The generalized Darcy's law was considered to determine the advective flow of liquid phase as follows:

$$\boldsymbol{q}_\alpha = -\frac{\boldsymbol{k}k_{\mathrm{r}\alpha}}{\mu_\alpha}\left(\nabla P_\alpha - \rho_\alpha \boldsymbol{g}\right)\ (\alpha = \mathrm{l,g}) \tag{3}$$

where $\boldsymbol{k}$ is the intrinsic permeability tensor (m^2), $k_{\mathrm{r}\alpha}$ is the relative permeability, μ_α is the dynamic viscosity (Pa s), P_α is the pressure (Pa), and $\boldsymbol{g}$ is the gravity acceleration. The intrinsic permeability tensor as a function of porosity can be defined by the Kozeny equation as

$$\boldsymbol{k} = \boldsymbol{k}_\mathrm{o}\left(\frac{\phi}{\phi_\mathrm{o}}\right)^3\left(\frac{1-\phi_\mathrm{o}}{1-\phi}\right)^2 \tag{4}$$

where ϕ_o is the reference porosity; and $\boldsymbol{k}_\mathrm{o}$ is the reference intrinsic permeability (m^2), which is assumed isotropic at the reference porosity. The retention curve model of van Genuchten (1980) was used:

$$S_\mathrm{e} = \frac{S_\mathrm{l} - S_\mathrm{rl}}{S_\mathrm{ls} - S_\mathrm{rl}} = \left\{1 + \left[\frac{P_\mathrm{g} - P_\mathrm{l}}{P_0\left(\sigma/\sigma_0\right)}\right]^{\frac{1}{1-\lambda}}\right\}^{-\lambda} \tag{5}$$

where S_e is the effective liquid saturation defined in terms of the residual liquid saturation (S_rl) and the maximum liquid saturation (S_ls); P_0

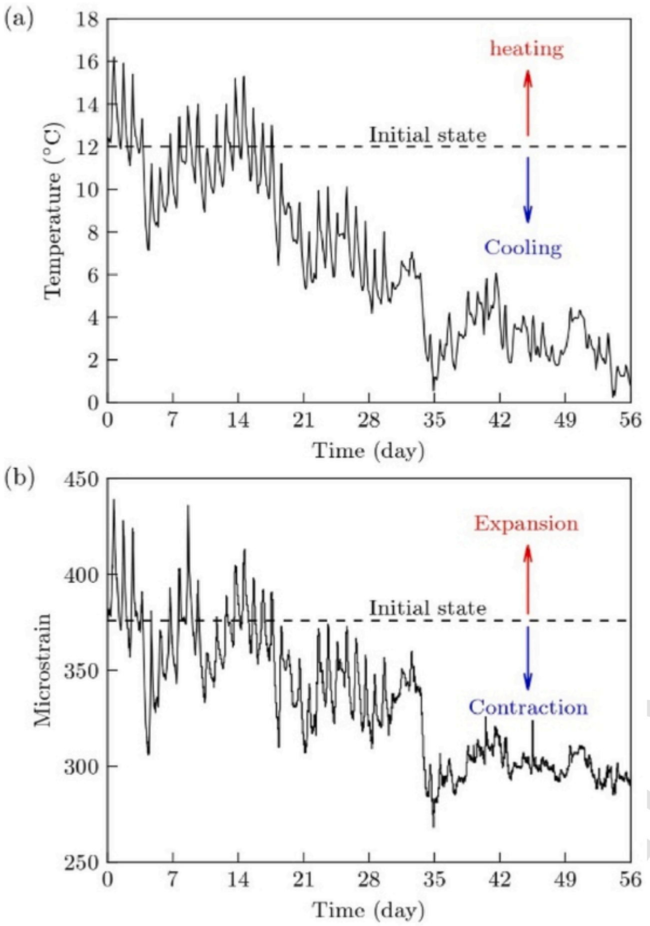

Fig. 4. In situ measurements, including air temperature and surface strain of the rock cliff.

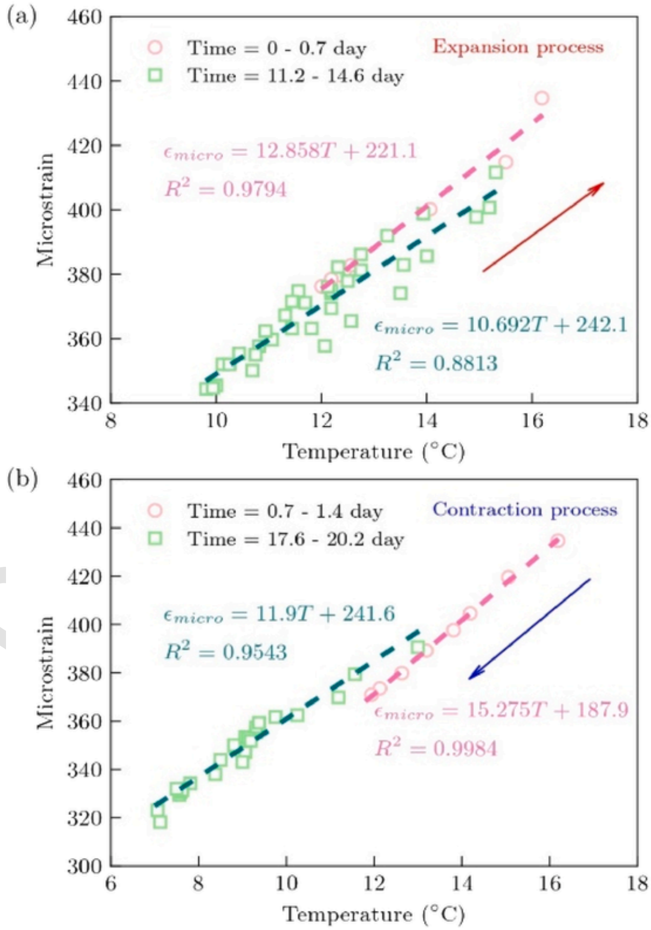

Fig. 5. Cyclic variations in microstrain–temperature relationship (a) during increasing temperature and rock expansion and (b) during decreasing temperature and rock contraction.

is the air entry value (Pa); σ is the surface tension (N/m) at a temperature T (∘ C); and σ_0 is the surface tension at a temperature, at which P_0 is measured. Furthermore, S_e controls the relative permeability to water through the following dependency:

$$k_{rl} = A S_e^{\Lambda} \tag{6}$$

where A is a constant, and Λ is the model parameter.

To consider conductive heat transfer through porous medium, Fourier's law is employed:

$$\boldsymbol{i}_c = -\lambda \nabla T \tag{7}$$

where λ is the thermal conductivity of the medium (W/(m K)). The values of these parameters used for the simulations are presented in Table 2.

3.3. Mechanical constitutive equations

The simulations employ a viscoplastic damage constitutive model, which is known for its ability to reproduce the hydro-mechanical behavior of rock. This model utilizes an enhanced elastoplastic concept, which has been specifically developed for both saturated and unsaturated argillaceous rocks (Mánica et al., 2016). The model encompasses essential components, including an elasticity law, plastic flow rule, hardening law, and yield condition. A generalized effective stress expression has been adopted:

$$\boldsymbol{\sigma}' = \boldsymbol{\sigma} + S_e s B \boldsymbol{I} \tag{8}$$

where $\boldsymbol{\sigma}'$ is the effective stress tensor, s is the suction, B is the Biot's coefficient, and $\boldsymbol{I}$ is the identity tensor. For saturated conditions, Eq. (8) reduces to

$$\boldsymbol{\sigma}' = \boldsymbol{\sigma} + P_l B \boldsymbol{I} \tag{9}$$

where the liquid pressure (P_l) is equal to $-s$.

Based on the elasticity law, the elastic stress–strain relationship is expressed as

$$\boldsymbol{\sigma} = \boldsymbol{D}_e \left(\varepsilon - \varepsilon_p\right) \tag{10}$$

where $\boldsymbol{\sigma}$ denotes the column matrix of independent stress components, $\boldsymbol{D}_e$ is the elastic stiffness matrix, ε is the column matrix of engineering total strain components, and ε_p is the column matrix of engineering plastic strain components.

The mechanical response of rock can be explained within the framework of elastoplasticity. At low deviatoric stresses, the behavior is linear elastic, characterized by a transverse isotropic version of Hooke's law. When subjected to higher deviatoric stresses, plastic deformations may occur. Three yield limits are considered: initial, peak, and residual. The initial limit defines a stress surface separating the elastic and plastic regions, allowing for further loading. The peak limit signifies the material's maximum strength. Subsequently, strength gradually dimin-

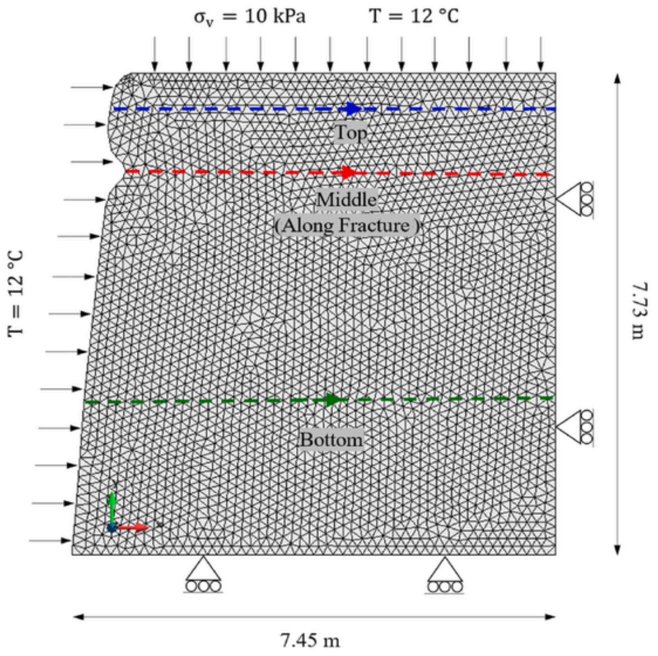

Fig. 6. Representation of the modeled domain, finite element mesh, and initial boundary conditions.

Table 2
Rock parameters used in the simulation.

Properties	Parameter	Value
Hydraulic	Intrinsic permeability, k_0 (m^2)	1.93×10^{-21}
	Material parameter, η	300
	Model parameter, P (MPa)	14.3
	Material parameter, λ	0.33
	Material parameter, A	1
	Material parameter, Λ	3
Hydro-mechanical	Biot's coefficient, B	0.6
Thermo-mechanical	Linear thermal expansion coefficient of the rock, α_T (K^{-1})	1.4×10^{-5}
Thermal	Thermal conductivity, λ (W/(m K))	2
	Specific heat capacity of the solid, c_s (J/(kg K))	800
Petrophysical	Solid compressibility, β_s	2.5×10^{-5}
	Specific weight, ρ_s (kg/m^3)	Table 1
	Porosity, ϕ	Table 1

ishes to its residual value, which is modeled through softening plasticity (Tourchi et al., 2021). The Mohr–Coulomb criterion is applied to the initial, peak, and residual limits, which is expressed in terms of commonly used stress invariants:

$$f = \left(\cos\ \theta + \frac{1}{\sqrt{3}} \sin\ \theta\ \sin\ \varphi \right) J - \left(p' + p_t \right) \sin\ \varphi \geq 0 \tag{11}$$

where θ, J, and p' are the stress invariants; φ is the friction angle; and p_t is the tensile strength, which is defined as a function of cohesion (c) and friction angle (φ):

$$p_t = c\ \cot\ \varphi \tag{12}$$

The initial yield limit is represented in Eq. (11) using initial material parameters φ_{ini} and c_{ini}. Similarly, the failure limit is determined by substituting φ and c with their peak values, denoted as φ_{peak} and c_{peak}. Nonlinear isotropic hardening is taken into account, driven by the evolution of the yield parameters. The state variable governing this evolution is identified as the equivalent plastic strain:

$$\varepsilon_{eq}^{p} = \left(\frac{2}{3} \varepsilon^{p} : \varepsilon^{p} \right)^{1/2} \tag{13}$$

Based on Mánica et al. (2016), the cohesion c and mobilized friction angle φ_{mob} first increase to a maximum value due to bonding effects, and then decrease to a residual value. Subsequently, a gradual reduction occurs until the residual strength is reached at significant displacements. Consequently, the values of $c\left(\varepsilon_p\right)$ and $\varphi\left(\varepsilon_p\right)$ will be determined using the initial yield, peak, and residual friction angles obtained from the stress–strain curve in triaxial tests as follows:

$$\varphi_{mob} = \varphi_{ini} + \frac{\varepsilon_{eq}^{p}}{a_{hard} + \left(\varepsilon_{eq}^{p} / \Delta\varphi_{hard} \right)} \tag{14}$$

$$\Delta\varphi_{hard} = \frac{\xi_1}{\left[\xi_1 / \left(\varphi_{peak} - \varphi_{ini} \right) \right] - a_{hard}} \tag{15}$$

$$\varphi_{mob} = \varphi_{peak} + \frac{\varepsilon_{eq}^{p} - \xi_2}{a_{soft} + \left[\left(\varepsilon_{eq}^{p} - \xi_2 \right) / \Delta\varphi_{soft} \right)]} \tag{16}$$

$$\Delta\varphi_{soft} = \frac{\xi_3 - \xi_2}{\left[\left(\xi_3 - \xi_2 \right) / \left(\varphi_{peak} - \varphi_{res} \right) \right] - a_{soft}} \tag{17}$$

where φ_{res} is the residual friction angle, ξ_1 is the equivalent plastic strain at which the maximum strength is reached, ξ_2 is the equivalent plastic strain at which softening begin, ξ_3 is the equivalent plastic strain at which the residual strength is reached, a_{hard} is the constant that controls the curvature of the function in the hardening branch, and a_{soft} is the constant that controls the curvature of the function in the softening branch, as shown in Fig. 7. Cohesion evolves in parallel with the friction angle according to the following equation:

$$c_{mob} = c_{peak}\ \cot\ \varphi_{ini}\ \tan\ \varphi_{mob} \tag{18}$$

where c_{mob} is the mobilized cohesion, and c_{peak} is the peak cohesion.

The model adopts a non-associated flow rule. Rather than deriving a specific function for plastic potential, the flow rule is obtained from the yield criterion in the following manner:

$$\frac{\partial g}{\partial \boldsymbol{\sigma}'} = \omega \frac{\partial f}{\partial p'} \frac{\partial p'}{\partial \boldsymbol{\sigma}'} + \frac{\partial f}{\partial J} \frac{\partial J}{\partial \boldsymbol{\sigma}'} + \frac{\partial f}{\partial \theta} \frac{\partial \theta}{\partial \boldsymbol{\sigma}'} \tag{19}$$

where g is the plastic potential, and ω is a constant that controls the volumetric component of plastic deformations. When $\omega = 1$, an associated flow rule is achieved, whereas with $\omega = 0$, there are no volumetric plas-

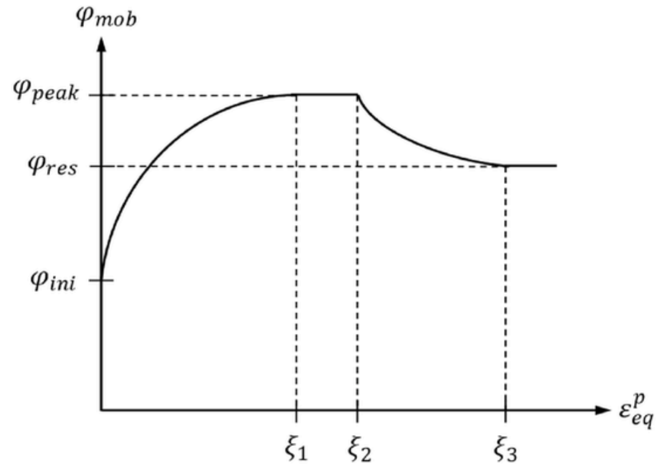

Fig. 7. Evolution of friction angle in hardening and softening regimes (Mánica et al., 2016).

tic strains. An appropriate value for geomaterials typically falls between these limits.

An additional mechanism is proposed for the time-dependent response, characterized by a modified form of Lemaitre's law:

$$d\varepsilon^{\mathrm{vp}} = \left(\frac{2}{3}\frac{\dot{\varepsilon}^{\mathrm{vp}}}{q}s\right)dt \tag{20}$$

$$q = \left(\frac{3}{2}s : s\right)^{1/2} \tag{21}$$

$$\dot{\varepsilon}^{\mathrm{vp}} = \gamma\left(q - \sigma_{\mathrm{s}}\right)^{n}\left(1 - \varepsilon_{\mathrm{eq}}^{\mathrm{vp}}\right)^{m} \tag{22}$$

where $d\varepsilon^{\mathrm{vp}}$ is the viscoplastic strain increment (time-dependent response), dt is the time increment, $\dot{\varepsilon}^{\mathrm{vp}}$ is the viscoplastic strain rate tensor, γ is a viscosity parameter, σ_{s} is a threshold from which viscoplastic strain is activated, n and m are material constants, and $\varepsilon_{\mathrm{eq}}^{\mathrm{vp}}$ is the state variable of the time-dependent response given by

$$\varepsilon_{\mathrm{eq}}^{\mathrm{vp}} = \int_0^t \left(\frac{2}{3}\dot{\varepsilon}^{\mathrm{vp}} : \varepsilon^{\mathrm{vp}}\right)^{1/2} dt \tag{23}$$

The parameters of the mechanical constitutive model used in the simulations are presented in Table 3. In this study, the parameters employed for the numerical model were determined through a combination of direct sampling and iterative calibration. Due to the absence of direct measurements of viscoplastic properties, an iterative calibration approach was employed. This method involves adjusting the numerical model parameters iteratively to achieve a good match between the numerical simulation results and the field measurements. The viscoplastic properties of the rock were estimated by comparing the field-measured data (such as strain changes due to thermal processes) with the numerical model outputs. This iterative process helped to fine-tune the parameters to ensure the model accurately reflects the observed behavior of the rock slope under varying environmental conditions. To validate the numerical model, the simulation results were compared with in situ measurements.

4. Results and discussion

4.1. Temperature distribution

Fig. 4a depicts the cyclic temperature variations, indicating that the rock slope is typically subjected to decreasing temperatures. Applying these temperature changes to the rock slope boundaries, the surface parts of the rock contribute to the temperature distribution within its mass based on the assigned thermal conductivity.

Fig. 8 compares the model results of temperature changes on the rock slope surface with in situ measurements. By matching the temperature results at the rock surface and ensuring the correct functionality of the numerical model, the temperature distribution within the rock slope mass can be investigated.

Since the upper parts of the slope are affected by the presence of the initial fracture and two boundaries exposed to temperature changes, they experience different temperature distributions compared to the lower parts of the slope. Therefore, to gain a more comprehensive understanding of the temperature changes in the rock mass due to air temperature changes, the temperature distributions for the top, middle, and bottom lines (as shown in Fig. 6) are illustrated in Fig. 9 at different times. The highest temperature (16.19 °C) recorded on day 0.7 and the lowest temperature (0.25 °C) on day 54.1 represents the temperature limits. By plotting temperature changes on different days, it is possible to determine the temperature variation range of the rock slope mass.

According to Fig. 9, the surface of the rock slope exhibits the most pronounced temperature variation range (0.25 °C-16.19 °C) because it is directly exposed to air temperature fluctuations. In general, as illustrated in all graphs of Fig. 9, moving toward the rock mass, temperature variations become more limited and reach a specific constant value. Fig. 9a shows the temperature changes in the lower part of the slope (bottom line). As observed, these changes reach zero at a distance of about 5 m from the surface, indicating that only the initial 5 m of the rock slope mass is affected by climatic changes.

The middle part of the slope, due to the presence of the initial fracture and proximity to the upper boundary, has a greater temperature variation range than the lower part (Fig. 9b). These temperature changes start from 15.94 °C (0.25 °C-16.19 °C) at the slope surface and reach 3 °C (9 °C-12 °C) at a distance of 5 m, and then remain constant. Similarly, the upper part (top line) of the slope experiences the largest temperature variation range, primarily due to the occurrence of heat transfer from the upper boundary (Fig. 9c). These changes start from 15.94 °C at the slope surface and reach more than 6 °C at a distance of 5 m. Fig. 9d shows the temperature variation ranges for all three parts of the rock slope, indicating the non-uniform temperature distribution across the slope.

The evolution of temperature over time is presented in Fig. 10. As can be observed, the temperature variations in the first 10 d are heterogeneous due to the continuous changes between warming and cooling processes relative to the initial temperature of 12 °C. However, from the temperature contours of the 20th day onwards, the temperature distrib-

Table 3
Mechanical constitutive law parameters used in the simulation (Tourchi et al., 2021).

Parameter	Value
Young's modulus, E (MPa)	Table 1
Poisson's ratio, ν	Table 1
Initial friction angle, φ_{ini} (°)	9.35
Peak friction angle, φ_{peak} (°)	22
Mobilized friction angle, φ_{res} (°)	14.74
Peak cohesion, c_{peak} (MPa)	3
Constant that controls the curvature of the function in the hardening branch, a_{hard}	0.0035
Constant that controls the curvature of the function in the softening branch, a_{soft}	0.07
Coefficient of non-associativity, ω	0.6
Equivalent plastic strain at which the maximum strength is reached, ξ_1	0.005
Equivalent plastic strain at which the residual strength is reached, ξ_3	0.006
The threshold from which viscoplastic strains are activated, σ_{s} (MPa)	4
Viscosity parameter, γ (d^{-1})	$1 \bullet 10^{-7}$
Material constants, m	530
Material constants, n	3.37

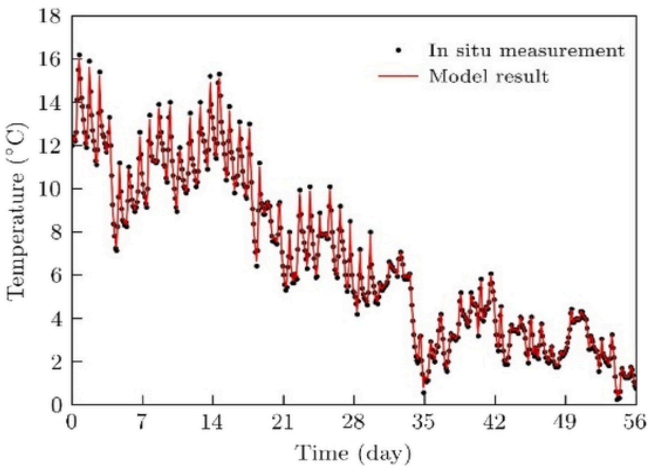

Fig. 8. Comparison between surface temperature variations of the rock cliff using in situ measurements and model results.

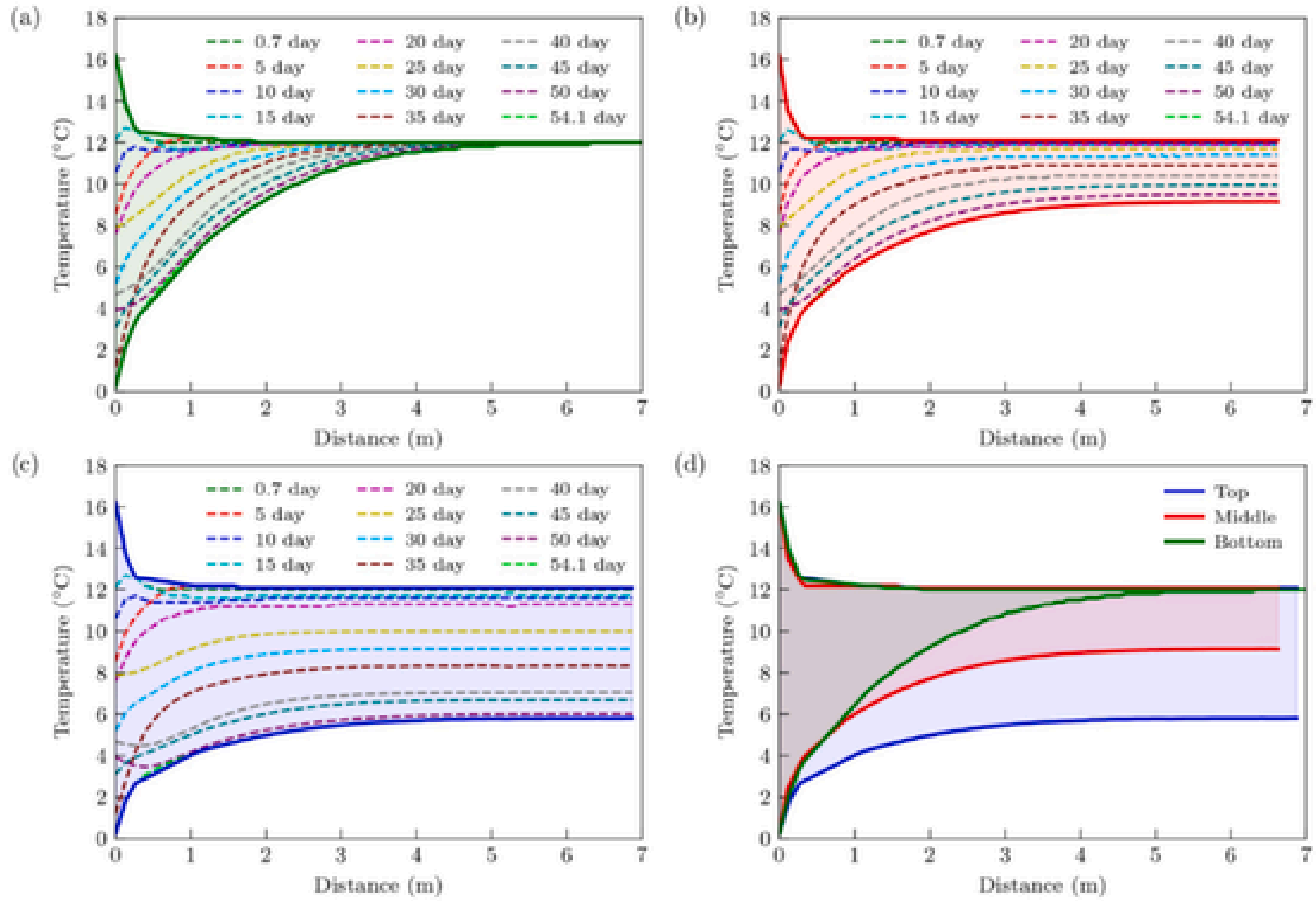

Fig. 9. Temperature distribution within the rock cliff mass: (a) along the bottom line, (b) along the middle line, (c) along the top line, and (d) showcasing the range of temperature variation in each line.

ution changes more uniformly, which shows the general trend of temperature reduction in the rock mass. The temperature distribution within the rock slope mass can have important implications for the stability of the slope. If the temperature changes too rapidly or unevenly, it can cause the rock to crack or break. This can lead to landslides or rockfalls.

4.2. *Strain evolution*

As shown in Fig. 4b, the overall trend of strain changes over time is downward, indicating contraction due to decreasing temperature. The microstrain is initially observed to be approximately 376.2 and subsequently exhibits fluctuations between the maximum and minimum values of 438.8 and 267.6, respectively. Based on field and laboratory studies, it was observed that the material properties vary significantly within short distances of the rock slope, which may be attributed to factors such as inhomogeneity, anisotropy, weathering, and non-uniform stress conditions. Therefore, sampling to determine material properties is not necessarily sufficient to investigate the behavior of the slope. Only the overall behavior of the slope can be studied relatively. To avoid the complexities of material and slope geometry, each property obtained from experimental tests was applied homogeneously throughout the entire domain.

Similar to temperature changes, microstrain was evaluated at three points: top, middle, and bottom (corresponding to the intersection of each line with the slope surface) to investigate the impact of different temperature distributions on surface strains. Fig. 11 presents a comparison between the strain changes of Models A, B, and C for three parts of the rock slope and field measurements. Generally, with increasing temperature, expansion occurs in the rock mass, resulting in increased microstrain and deformation in the opposite direction of the x-axis, as illustrated in Fig. 6. Conversely, with decreasing temperature, the rock contracts, and the microstrain direction aligns with the x-axis, as shown in Fig. 6.

As shown in Fig. 11a, the strain changes are almost identical throughout the slope surface until day 28. However, after day 28, the trend of strain changes in all three sections changes, with the top and middle points experiencing a more severe strain decrease on day 35 and deviating from the measured values for a specific level of the rock slope. Meanwhile, the downward trend observed at the bottom point continues along the measured values. This abrupt decrease in strain can be attributed to a sudden decline in temperature in a few days. Additionally, except for the pronounced decrease observed in Model A on day 35, strain fluctuations are less pronounced compared to Models B and C due to the high elastic modulus and very low porosity of Material A, which results in a reduced rate of changes. However, at first glance, it can be claimed that the rock slope comprising highly rigid material and minimal porosity in the vicinity and above the initial fracture has transitioned from an elastic behavior to an irreversible deformation phase.

The strain changes of Model B in Fig. 11b show different results compared to Model A. Due to the lower elastic modulus and higher porosity of Model B compared to Model A, greater fluctuations are possible due to temperature changes. Therefore, Model B is more aligned with field measurements than Model A. Another difference between

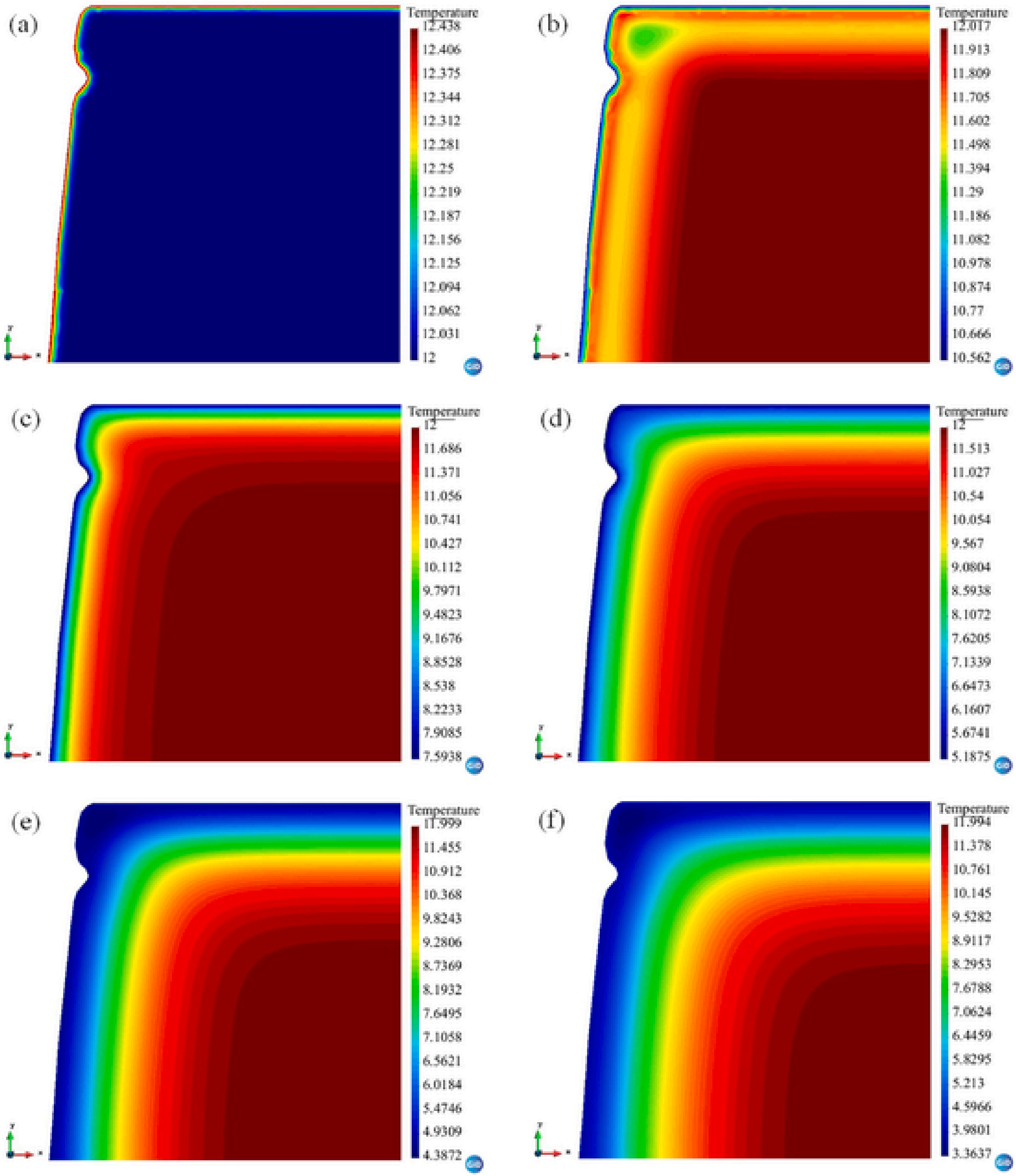

Fig. 10. Temperature evolution within rock slope mass after (a) 0.1 d, (b) 10 d, (c) 20 d, (d) 30 d, (e) 40 d, and (f) 50 d.

Models B and A is the slope behavior observed after day 35. Although all models show a significant decrease in strain on day 35, no sudden change in behavior is observed in any part of the slope in Model B, and the behavior changes gradually. Until day 21 (3 weeks after the start of temperature changes), the strain changes are almost identical throughout the slope surface. However, after that, the trend of strain changes in the three different parts of the slope becomes distinct, indicating different behaviors in distinct parts of the rock slope. Thus far, the lower section of Model B more closely approximates the observed behavior of the rock.

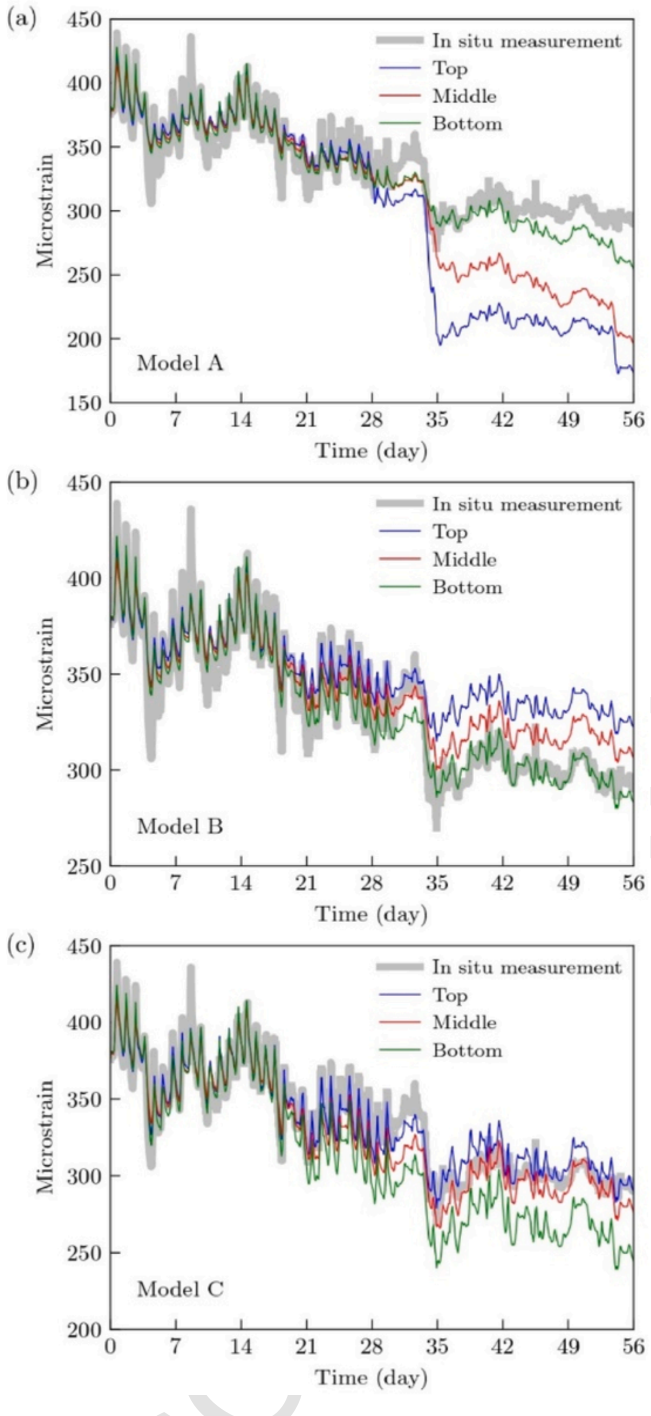

Fig. 11. Comparison between in situ measurement of microstrain and model results: (a) Model A; (b) Model B; and (c) Model C.

As shown in Fig. 11c, Model C, exhibiting the lowest elastic modulus and highest porosity among all the models, predicts strain changes better than the other two models. Similarly, the trends are consistent for a certain period of about 21 d, after which the behavior in the three different parts of the slope becomes different.

In general, the short- and long-term behaviors of materials differ due to their fundamental visco-elastoplastic characteristics. Material A, characterized by its high stiffness (e.g. Young's modulus) and strength, initially exhibits superior resistance to temperature-induced strains during the early stages (up to 35 d). This observation aligns with classic elasticity theory, which posits that stiffer materials experience less deformation under a given stress. Therefore, Model A demonstrates smaller strain changes compared to Models B and C, which possess lower stiffness values.

However, this initial advantage may not be sustained over the long term. The higher the stiffness of a material, the lower its ductility (i.e. its capacity for plastic deformation), and the greater its brittleness. These properties render the material more susceptible to delayed failure mechanisms such as creep and fatigue when subjected to sustained environmental stressors like temperature fluctuations. While Models B and C exhibit good ductility over the period studied, their lower initial stiffness might suggest higher long-term resilience due to their capacity for plastic deformation and energy absorption. Further clarification of this behavior could be obtained from future long-term simulations or creep tests.

The mechanisms of delayed failure can be elaborated with phenomena such as microcrack initiation and propagation, creep and fatigue, and cyclic thermal expansion and contraction. In stiffer and more brittle materials like Model A, microcracks tend to initiate earlier and propagate more rapidly when subjected to cyclic temperature variations. The limited ductility means that these materials cannot undergo significant plastic deformation to redistribute stress, leading to the accumulation of localized stresses at crack tips. Over time, these microcracks coalesce and propagate, leading to macro-scale fractures and potential failure. This can be defined as delayed failure, given that in the early stages, stiffer rock displays a greater resistance to environmental stressors, with the sudden failure occurring later. Moreover, creep refers to the time-dependent deformation under sustained load, while fatigue signifies the progressive and localized structural damage that occurs under cyclic loading. In the context of Model A, the material's higher brittleness and lower ductility mean that it is less capable of withstanding prolonged thermal cycling without accumulating damage. Microcrack growth under cyclic thermal stress can progressively weaken the rock structure, making it more prone to sudden brittle failure after a critical period. In addition, repeated cycles of thermal expansion and contraction exacerbate the growth of microcracks. In more ductile materials such as Models B and C, the rock can accommodate these expansions and contractions through plastic deformation, reducing the stress concentration at crack tips. However, in Model A, the lack of plasticity means that thermal stresses concentrate more intensely, accelerating crack propagation.

The observed differences highlight the importance of considering both short- and long-term material properties when evaluating the stability of rock slopes under environmental loading. This necessitates incorporating visco-elastoplastic material models in numerical simulations to capture the time-dependent response of rock slopes to temperature changes and other environmental factors.

4.3. Propagation of the fracture zone

To further investigate the long-term behavior of the rock slope under temperature changes in Model A, it is necessary to evaluate the damage zone (i.e. fractured zone). Fig. 12 presents the contours of the plastic multiplier, an indicator of the damage zone as mentioned by Tourchi et al. (2021, 2023), for Model A over time. As illustrated in Fig. 12a and b, the surface damage commences from the lower parts and around the initial fracture. With continuous temperature changes, the fractured zone extends in all directions, with the extension being more significant in the upper parts. Notably, the upper slope section becomes highly susceptible to cracking and environmental damage in the later stages. The most vulnerable part of the rock slope in response to temperature changes is the upper section above the initial crack, which is referred to as the critical fractured zone (CFZ).

This zone initiates on day 30, encompassing a small area, and gradually expands over time, forming the CFZ. The formation of the CFZ is a

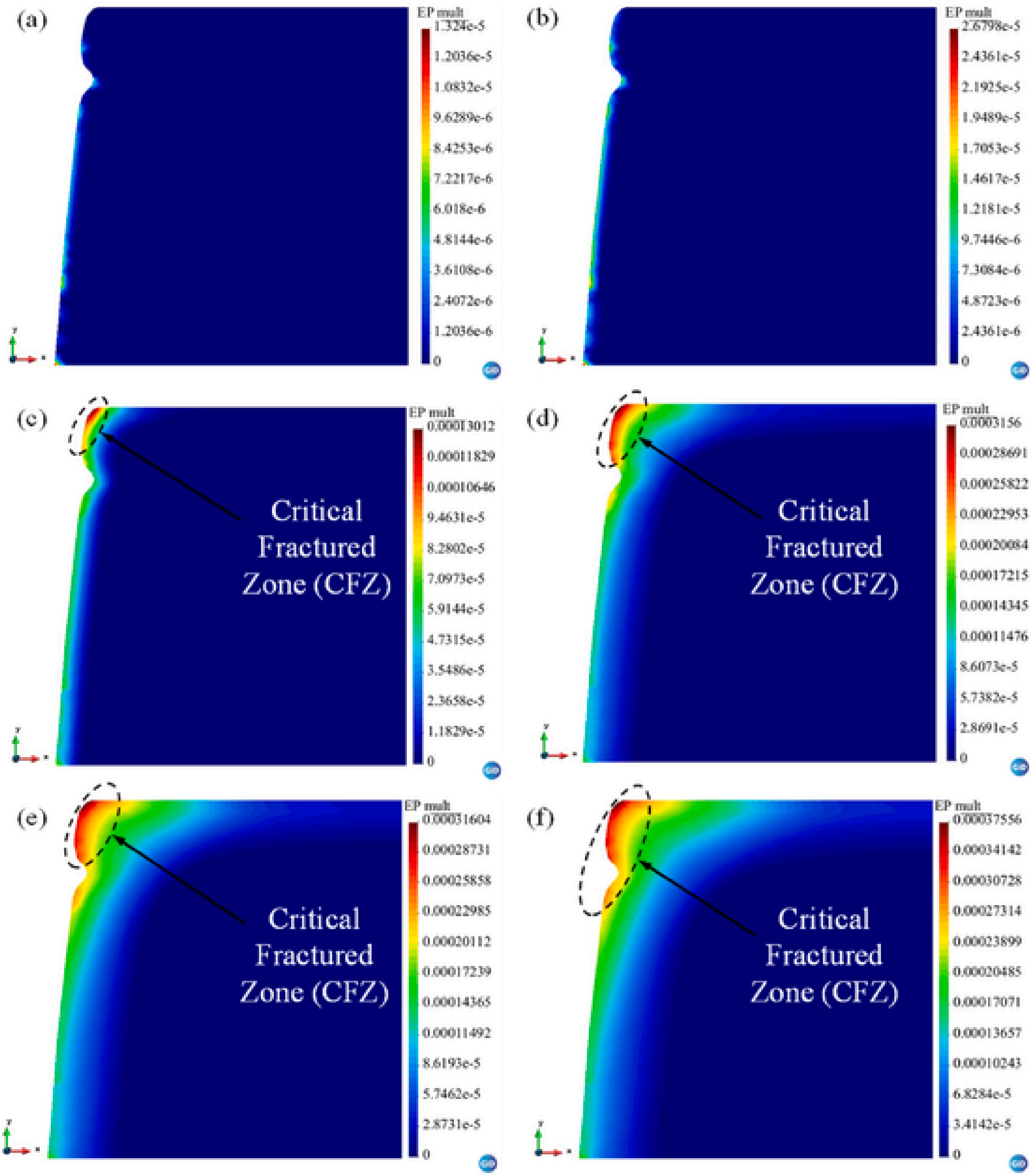

Fig. 12. Configuration of the fractured zone obtained in terms of the plastic multiplier for Model A in (a) 10 d, (b) 20 d, (c) 30 d, (d) 40 d, (e) 50 d, and (f) 56 d.

critical event in the long-term behavior of the rock slope, as it can lead to significant instability and failure. Concerning the impact of crack growth in the damaged zone on permeability, Fig. 13a illustrates the evolution of permeability within the damaged zone. The numerical results reveal an increase in permeability, suggesting the potential for the formation of cracks or micro-cracks in the rock mass due to thermal deformations. These cracks provide preferential pathways for fluid flow, which can increase the hydraulic conductivity of the rock mass and lead to water infiltration and seepage.

When subjected to decreasing temperature, rock contraction occurs due to thermal effects. As the temperature decreases, the pore volume of the rock mass reduces, which increases the pore water pressure. This

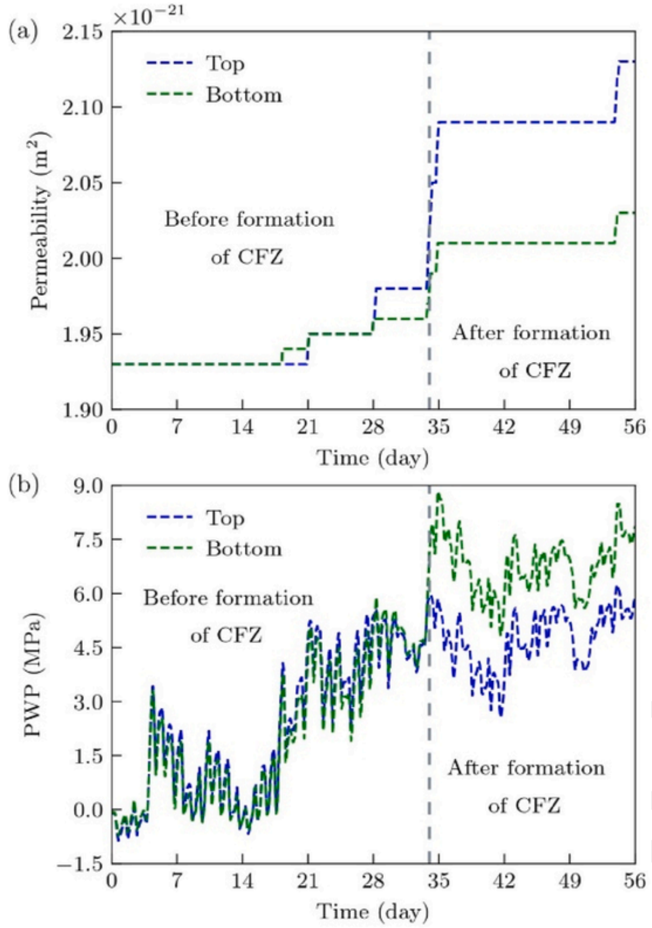

Fig. 13. (a) Permeability and (b) pore water pressure evolution before and after the formation of CFZ in Model A.

can further reduce the effective strength of the rock mass and exacerbate the damage and cracking process.

Fig. 13b demonstrates that the pore water pressure is rising in the damaged zone in both the lower and upper parts of the rock slope. However, it is of paramount importance to differentiate this phenomenon from the period of CFZ formation. As can be observed, after the formation of the CFZ, the pore water pressure in the top point is lower than that in the bottom point. This is because the cracks and micro-cracks in the upper part provide pathways for pore water dissipation, which reduces the pore water pressure. Therefore, it can be inferred that the reason for the sharp strain change in Model A in Fig. 11a in the upper part of the rock slope is the formation of the CFZ. The CFZ reduces the load-carrying capacity of the rock mass and leads to a sudden increase in strain.

Fig. 14 shows the fractured zone represented by the plastic multiplier for Model B. As can be observed, the damaged zone in Model B originates from the initial crack location and begins to expand from the lower part after 56 days. It is also noteworthy that in Model A, the damaged zone started to form around the fourth day, while in Model B, this zone formed after 34 d. Furthermore, no damaged zone was observed in Model C, which is likely because stiffer materials have lower ductility and are more prone to brittle failure under sustained loading.

To further investigate the influence of temperature changes on fracture zone propagation, the plastic multiplier for Models A and B is presented in Fig. 15, with a particular focus on the damaged areas. As observed in Fig. 15a, the damage zone in Model A initiates around day 4 across the entire slope surface and subsequently expands with time. As mentioned earlier, the plastic multiplier changes in the upper, middle, and lower parts of the slope are approximately similar until day 34. However, a significant extension of the damaged zone occurs between days 34 and 35, with the plastic multiplier increasing by 2.5–3 times during this period. Overall, according to Fig. 15a and the contours of Fig. 12, the CFZ with the highest plastic multiplier value forms at the top point and decreases downward along the slope surface.

According to Fig. 15b, the formation and subsequent expansion of the damaged zone in Model B commences from day 34 onwards. A comparison of the formation and extension of the damaged zone in Models A and B, reveals that the plastic multiplier values in the middle and bottom points of the slope in Model A are approximately 10 times those in Model B. Additionally, the temporal extension of the damaged zone in Model A occurs in approximately five stages, while in Model B, it occurs in only two stages.

A similar significant change occurs at day 34, where the plastic multiplier increment (PMI) is denoted by PMI_t where t is the time at which PMI ceases and continues constantly. The PMI_t variations for different slope sections in Models A and B are shown in Fig. 16.

As can be observed, the damaged zone in Model A initiates in the middle (initial fracture) and bottom points, similar to Model B. With the

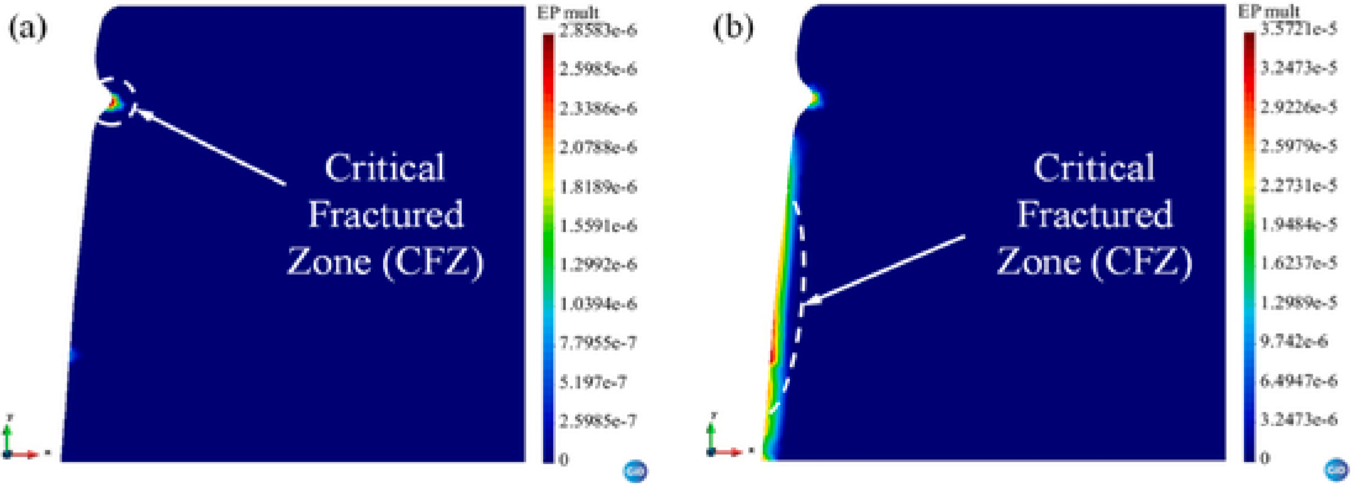

Fig. 14. Configuration of the fractured zone obtained in terms of the plastic multiplier for Model B in (a) 34 d and (b) 56 d.

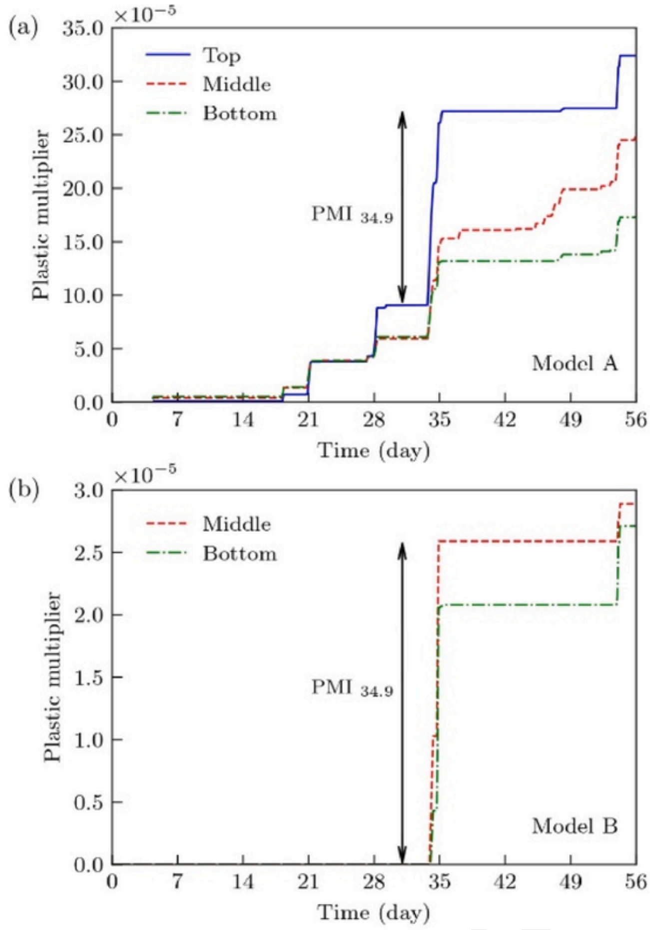

Fig. 15. Fractured zone evolution in terms of the plastic multiplier at different points of the top, middle, and bottom parts for (a) Model A and (b) Model B.

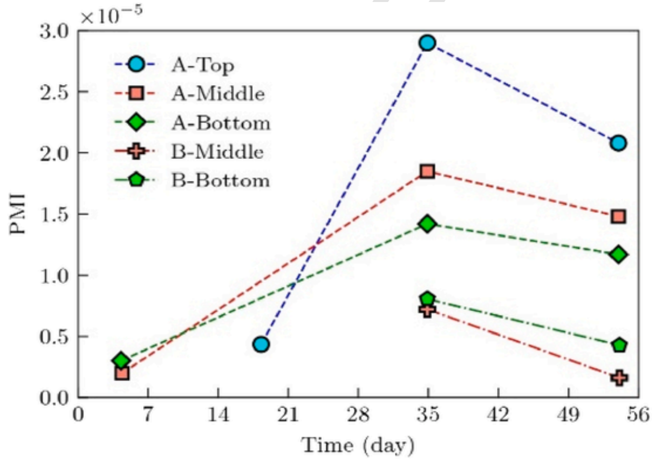

Fig. 16. PMI evolution at different points of the top, middle, and bottom parts of rock surface for Models A and B.

elapsed time, the damaged zone in the upper part of the slope forms at day 18.2. The results show that the propagation rate of the damaged zone in Model A is considerably higher at the top point than at the middle point and slightly higher at the middle point than at the bottom point. In other words, although the damaged zone in the upper part forms later, it expands rapidly after its formation. After day 34.9, when the extension that started on day 34 ends, the damaged zone expands at a slower rate. The initiation and propagation of cracks in the rock mass are primarily governed by the tensile stresses induced by thermal contraction. Stress concentration at the tip of pre-existing cracks, such as the initial fracture in slope geometry, intensifies tensile stresses, leading to early crack initiation and rapid propagation.

In contrast to Model A, the PMI comparison in Model B shows that the propagation rate of the damaged zone in the lower part of the slope is higher than that in the middle part. Similar to Model A, Model B experiences its maximum PMI on day 34.9 and then expands at a slower rate. Due to the distinct behavior of the rock slope with different materials, the damaged zone penetrates different distances from the slope surface into the rock mass. This factor is important because it can put different parts of the slope on the verge of failure and instability, providing valuable insights into the long-term behavior of the slope. Therefore, based on the results of Figs. 12 and 14, the extent of fractured zone penetration into the rock mass is presented in Fig. 17, which illustrates the distance of damaged zone extension from the slope surface.

As observed in Fig. 12, the damaged zone in the upper part of Model A extends to the right boundary of the model geometry. Accordingly, this value is not depicted in Fig. 17, as this part of the slope represents the complete extension of the fractured zone. By comparing the damaged zone penetration distance from the slope surface in the middle and bottom parts of the slope in Models A and B, it can be concluded that in the middle part of Model A, the damaged zone has extended up to 4.74 m from the initial fracture tip, representing the highest value among all other parts. This is followed by the lower part of Model A, where the rock mass has been subjected to temperature changes up to 1.91 m, resulting in changes in material properties and behavior such as increased permeability.

Conversely, Model B exhibits the highest extension at the end of 56 d, with a penetration depth of 0.32 m, in the lower part, which is almost halved in the middle part of the slope, where the damaged zone extends up to 0.17 m from the initial fracture tip. The results demonstrate that the geometrical asymmetry of the slope due to the presence of the initial fracture, in addition to the material property differences, has a significant impact on the initiation and propagation pattern of the damaged zone.

4.4. Porosity evolution

As mentioned in Section 4.2, rock subjected to temperature changes undergoes continuous thermal expansion and contraction, which can

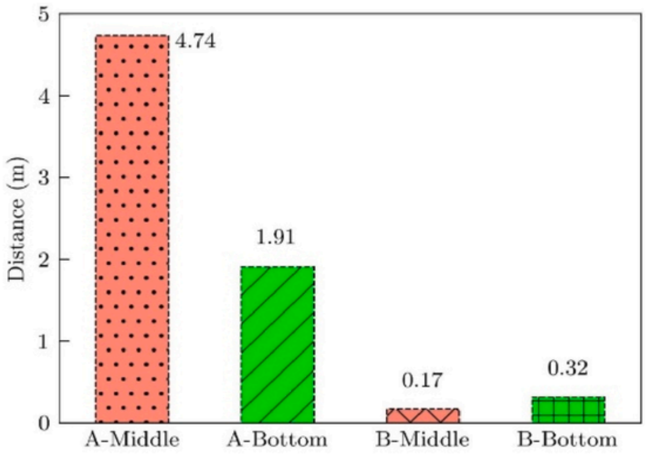

Fig. 17. The progress distance of the fractured zone at different points from the rock surface.

alter its long-term behavior due to phenomena such as fatigue or surface microcracks propagating within the rock mass. To investigate the volumetric changes of the rock at the slope surface, the temporal variations in porosity relative to its initial value ($\Delta\phi = \left[(\phi - \phi_0)/\phi_0\right] \times 100\%$) in each model were presented in Fig. 18 along with the temperature changes.

In general, an initial temperature increase induces thermal expansion in the rock, increasing its volume and porosity (positive $\Delta\phi$). Over time, the temperature decreases, and the rock undergoes thermal contraction, decreasing its volume and porosity (negative $\Delta\phi$). The surface of the rock slope in all models experiences the greatest thermal expansion on day 0.7 at a temperature of 16.19 °C and the greatest thermal contraction on day 54.3 at a temperature of 0.31 °C. More precisely, in Model A, the porosity increases by 0.34% on day 0.7 and decreases by 1% on day 54.3 compared to its initial state. These values for Model B on days 0.7 and 54.3 are a 0.21% increase and a 0.55% decrease, respectively, while for Model C, they are a 0.11% increase and a 0.38% decrease, respectively.

These results demonstrate that although Model C experiences larger volumetric fluctuations due to temperature changes compared to the other models due to its more deformable material, its porosity changes relative to its initial state are smaller than those of the other models. This implies that the rock slope in Model C exhibits greater elastic behavior and less permanent deformation. Conversely, although Model A experiences smaller volumetric changes due to temperature changes because of its stiffer material, it exhibits the highest porosity changes because more plastic deformation occurs in the rock. Model B, which has a material that is more deformable than Model A and stiffer than Model C, shows an intermediate behavior.

5. Limitations and future scopes

The limitations of this study can be divided into two aspects. Firstly, the lack of real data has led to assumptions being made in some cases regarding the inputs to the model. Secondly, the numerical model itself has certain inherent limitations. In this study, due to the complexities of sampling and laboratory experiments on rocks, only the elastic properties of the rock, along with some material characteristics including solid phase density and porosity, were considered. Therefore, the viscoplastic properties of the material were selected from similar studies to ensure adequate correspondence between field-measured results and numerical model outputs.

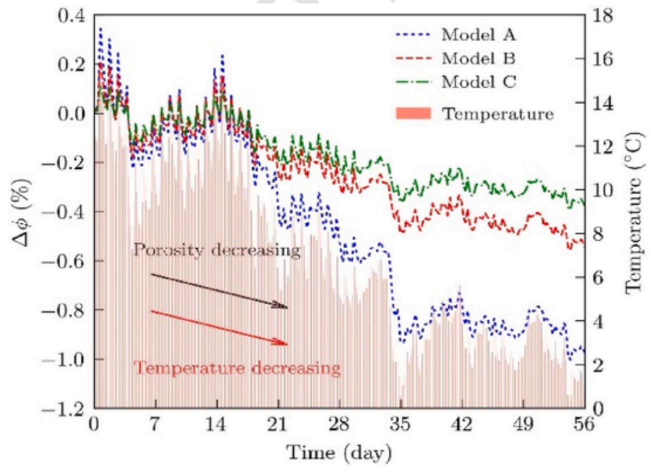

Fig. 18. Porosity changes at the bottom point on the surface of the rock cliff due to temperature variations in Models A, B, and C.

Moreover, based on field observations, the studied rock slope contains microcracks. However, the numerical model does not account for embedded cracks that existed in the initial conditions. Additionally, the model's boundary conditions are another factor. Due to the lack of available data regarding the initial conditions of pore pressure distribution, this study assumes that the rock medium is saturated for simplicity. Consequently, the boundary between the rock mass and the atmosphere has a pore water pressure of zero, acting as the water table.

The study is limited in scope to further differentiate the short- and long-term behavior of rocks with distinct properties under environmental stressors. Further research could focus on conducting more in-depth long-term simulations or creep tests to better understand the long-term behavior and failure modes of the materials. Future research could also explore systematic sensitivity analyses to understand the relative importance of various materials and environmental parameters on the THM response of rock slopes. Additionally, focus can be placed on developing constitutive models that can accurately capture the viscoelastoplastic behavior of rock materials and its impact on long-term slope stability. This could be achieved by enhancing the model through the integration of more extensive field data, including in situ measurements of pore pressure, temperature, and deformation over longer periods. This would improve the accuracy of the initial and boundary conditions used in the numerical model. Further studies on the initiation and propagation of microcracks in different rock types could be conducted. An understanding of how microcracks develop under cyclic thermal stress could provide insights into the delayed failure mechanisms observed in stiffer, more brittle materials like those in Model A presented in this study.

6. Conclusions

In this study, a comprehensive, fully coupled THM simulation of a rock slope situated in the Požáry test site was conducted. Field tests, which involved the instrumentation of the rock surface to measure strain changes under temperature variations, were complemented by laboratory sampling of the rock slope to measure its mechanical properties. The experimental findings highlighted the significant variability of rock properties, even over short distances.

The numerical simulations employed the precise geometry of the rock slope, as derived from field measurements, and incorporated a pre-existing fracture in the upper part of the rock slope surface. The temperature changes were assigned as boundary conditions to the exposed rock surfaces. The integration of key constitutive models, including the generalized Darcy's law for advective fluid flow, Fick's law for non-advective vapor flow, and Fourier's law for heat conduction was undertaken. The model considered porosity-dependent permeability and water retention curve. Additionally, a viscoplastic hardening-softening constitutive model with creep was employed to represent the long-term behavior of the rock slope under thermal loading. The mechanical constitutive model incorporates a dependency of permeability on rock damage via the plastic multiplier to simulate rock fracturing and its propagation, leading to the formation of a fractured zone.

The temperature results obtained from the model were compared with the corresponding in situ measurements. The findings revealed that the upper sections (top line) exhibited more extensive thermal changes than the lower parts, which can be attributed to the presence of a greater number of rock boundaries exposed to thermal effects. Specifically, at a distance of 5 m from the rock mass, the temperature at the top line was 3 °C higher than that at the middle line and 6 °C higher than that at the bottom line. Furthermore, the study of temperature-induced strain variations, in comparison with in situ measurements, revealed that Model A characterized by a stiffer material and lower initial porosity, exhibited lower strain changes within the initial 30 d. Conversely, Model C, with greater ductility in a specific thermal loading path, showed the most significant strain changes initially.

Beyond the initial 30 days, differences in rock slope behavior were observed between the various material types. Notably, a sudden decrease in strain trends occurred between days 34 and 35, particularly in Model A, where thermal contraction increased tensile stress, leading to damage such as fracturing and increased permeability. The investigation into damaged zones, specifically the CFZ, elucidated that a reduction in temperature resulted in contraction of the rock, leading to increased pore water pressure and exacerbating damage and cracking processes. The formation of the CFZ in Model A was associated with a sudden increase in strain, indicating a reduction in load-carrying capacity. The propagation rate of the damaged zone in Model A was significantly higher in the upper part, expanding rapidly after its formation.

In contrast, Model B exhibited a different pattern, with a higher propagation rate of the damaged zone in the lower part than that in the middle part. The PMI comparison in Model B indicated that, unlike Model A, the damaged zone in the lower part expanded more rapidly, reaching its maximum value on day 34.9 and then slowing down. A comparative analysis of the damaged zone penetration distances in Models A and B revealed that the upper part of Model A experienced the highest extension, reaching the right boundary of the model. Subsequently, the middle part of Model A experienced an extension of 4.74 m from the initial fracture tip.

As time elapsed, the rock underwent thermal contraction, reducing volume and porosity. The highest thermal expansion occurred on day 0.7, while the maximum thermal contraction occurred on day 54.3. Despite exhibiting smaller strain evolution in the initial 30 d, Model A exhibited the highest porosity changes, indicating more plastic deformation. Model C, despite displaying larger thermal strain fluctuations, demonstrated smaller porosity changes, suggesting more elastic behavior. Model B, with intermediate characteristics, demonstrated an intermediate response to temperature-induced variations.

CRediT authorship contribution statement

Saeed Tourchi: Writing – review & editing, Software, Resources, Conceptualization. **Milad Jabbarzadeh:** Writing – original draft, Visualization, Validation, Software, Methodology, Investigation, Conceptualization. **Arash Alimardani Lavasan:** Writing – review & editing. **Hamed Sadeghi:** Writing – review & editing. **Ondřej Racek:** Writing – review & editing, Resources.

Data availability statement

The data that support the findings of this study are available from the corresponding author upon reasonable request.

Declaration of competing interest

The authors declare that they have no known competing financial interests or personal relationships that could have appeared to influence the work reported in this paper.

Acknowledgements

The authors acknowledge financial support from the European Commission via a Marie Curie Fellowship (Grant No. 101033084) awarded to Dr. Saeed Tourchi (corresponding author). The second author is grateful to the Research Grant Office at Sharif University of Technology for grants G4010902 and QB020105. The last author acknowledges funding from the TAČR project SS02030023, "Rock Environment and Resources," under the "Environment for Life" program.

Nomenclature

ψ	Property per unit mass
ρ	Density
j_ψ	Total mass flux
f^ψ	Rate of production/decay of ψ per unit volume
θ_ψ	Volumetric mass of a species in a phase
ω_ψ	Mass fraction of that species
$\boldsymbol{\sigma}$	Stress tensor
$\boldsymbol{b}$	Vector of body forces
$\boldsymbol{q}$	Advective flow
$\boldsymbol{k}$	Intrinsic permeability tensor
k_r	Relative permeability
μ	Dynamic viscosity
P_l	Liquid pressure
P_g	Gas pressure
$\boldsymbol{g}$	Gravity acceleration
ϕ_o	Reference porosity
S_e	Effective liquid saturation
S_rl	Residual liquid saturation
S_ls	Maximum liquid saturation
P_0	Air entry value
σ	Surface tension
$\boldsymbol{i}_\mathrm{c}$	Conductive heat flux
λ	Thermal conductivity
$\boldsymbol{\sigma}'$	Effective stress tensor
s	Suction
B	Biot's coefficient
$\boldsymbol{I}$	Identity tensor
$\Delta\phi$	Variations in porosity relative to its initial value
$\boldsymbol{D}_\mathrm{e}$	Elastic stiffness matrix
ε	Column matrix of engineering total strain components
ε_p	Column matrix of engineering plastic strain components
θ, J, p'	Stress invariants

φ	Friction angle
p_{t}	Tensile strength
c	Cohesion
$\varepsilon_{\mathrm{eq}}^{\mathrm{p}}$	Equivalent plastic strain
φ_{mob}	Mobilized friction angle
φ_{res}	Residual friction angle
ξ_1	Equivalent plastic strain at which the maximum strength is reached
ξ_2	Equivalent plastic strain at which softening begin
ξ_3	Equivalent plastic strain at which the residual strength is reached
a_{hard}	Constant that controls the curvature of the function in the hardening branch
a_{soft}	Constant that controls the curvature of the function in the softening branch
g	Plastic potential
ω	Constant that controls the volumetric component of plastic deformations
$\varepsilon^{\mathrm{vp}}$	Visco-plastic strain
t	Time
$\dot{\varepsilon}^{\mathrm{vp}}$	Visco-plastic strain rate tensor
γ	Viscosity parameter
E	Young's modulus
ν	Poisson's ratio
CFZ	Critical Fractured Zone
PWP	Pore water pressure
PMI	Plastic multiplier increment

References

Alonso E.E., Zervos A., Pinyol N.M. Thermo-poro-mechanical analysis of landslides: from creeping behaviour to catastrophic failure. Geotechnique 2016;66(3):202–19.

Chen L.W.C.P., Wang C.P., Liu J.F., Li Y., Liu J., Wang J. Effects of temperature and stress on the time-dependent behavior of Beishan granite. Int. J. Rock Mech. Min. Sci. 2017;93:316–23.

Collins B.D., Znidarcic D. Stability analyses of rainfall induced landslides. J. Geotech. Geoenviron. Eng. 2004;130(4):362–72.

Gens A., Olivella S. THM phenomena in saturated and unsaturated porous media: fundamentals and formulation. Revue Française de géNie Civil 2001;5(6):693–717.

Ghandilou M.J., Tourchi S., Sadeghi H. Numerical investigation of cyclic wetting and drying of Boom clay based on the Barcelona Expansive Model. 84th EAGE Annual Conference and Exhibition, vol. 2023. European Association of Geoscientists and Engineers; 2023. https://doi.org/10.3997/2214-4609.202310400.

Gomah M.E., Li G., Sun C., et al. Macroscopic and microscopic research on Egyptian granodiorite behavior exposed to the various heating and cooling strategies. Geomech. Geophys. Geo-Energy Geo-Resour. 2022;8(5):158.

Gunzburger Y., Merrien-Soukatchoff V., Guglielmi Y. Influence of daily surface temperature fluctuations on rock slope stability: case study of the Rochers de Valabres slope (France). Int. J. Rock Mech. Min. Sci. 2005;42(3):331–49.

Hugentobler M., Aaron J., Loew S. Rock slope temperature evolution and micrometer-scale deformation at a retreating glacier margin. J. Geophys. Res.: Earth Surf. 2021; 126(11):e2021JF006195.

Jabbarzadeh M., Sadeghi H., Tourchi S., Darzi A.G. Thermo-hydraulic analysis of desiccation cracked soil strata considering ground temperature and moisture dynamics under the influence of soil-atmosphere interactions. Geomech. Energy Environ. 2024;38:100558.

Kumari W.G.P., Ranjith P.G., Perera M.S.A., Chen B.K., Abdulagatov I.M. Temperature-dependent mechanical behaviour of Australian Strathbogie granite with different cooling treatments. Eng. Geol. 2017;229:31–44.

Lan H., Zhao X., Macciotta R., et al. The cyclic expansion and contraction characteristics of a loess slope and implications for slope stability. Sci. Rep. 2021;11(1):2250.

Mánica M., Gens A., Vaunat J., Ruiz D.F. A time-dependent anisotropic model for argillaceous rocks. Application to an underground excavation in Callovo-Oxfordian claystone. Comput. Geotech. 2016;85:341–50.

Marmoni G.M., Fiorucci M., Grechi G., Martino S. Modelling of thermo-mechanical effects in a rock quarry wall induced by near-surface temperature fluctuations. Int. J. Rock Mech. Min. Sci. 2020;134:104440.

Mufundirwa A., Fujii Y., Kodama N., Kodama J.I. Analysis of natural rock slope deformations under temperature variation: a case from a cool temperate region in Japan. Cold Reg. Sci. Technol. 2011;65(3):488–500.

Olivella S., Carrera J., Gens A., Alonso E.E. Nonisothermal multiphase flow of brine and gas through saline media. Transport Porous Media 1994;15:271–93.

Olivella S., Gens A., Carrera J., Alonso E.E. Numerical formulation for a simulator (CODE_BRIGHT) for the coupled analysis of saline media. Eng. Comput. 1996;13(7): 87–112.

Panday S., Corapcioglu M.Y. Reservoir transport equations by compositional approach. Transport Porous Media 1989;4:369–93.

Park D.S., Shin M.B., Park W.J., Seo Y.K. Slope stability analysis model for the frost-susceptible soil based on thermal-hydro-mechanical coupling. Comput. Geotech. 2023;163:105715.

Racek O., Balek J., Loche M., Vích D., Blahůt J. Rock surface strain in situ monitoring affected by temperature changes at the Požáry field lab (Czechia). Sensors 2023;23 (4):2237.

Rodrıguez C.E., Bommer J.J., Chandler R.J. Earthquake-induced landslides: 1980–1997. Soil Dynam. Earthq. Eng. 1999;18(5):325–46.

Scaringi G., Loche M. A thermo-hydro-mechanical approach to soil slope stability under climate change. Geomorphology 2022;401:108108.

Sultan N., Delage P., Cui Y.J. Temperature effects on the volume change behaviour of Boom clay. Eng. Geol. 2002;64(2–3):135–45.

Sun B., Yang H., Fan J., Liu X., Zeng S. Energy evolution and damage characteristics of rock materials under different cyclic loading and unloading paths. Buildings 2023;13 (1):238.

Tang A.M., Cui Y.J., Barnel N. Thermo-mechanical behaviour of a compacted swelling clay. Geotechnique 2008;58(1):45–54.

Thota S.K., Vahedifard F. Stability analysis of unsaturated slopes under elevated temperatures. Eng. Geol. 2021;293:106317.

Tian X., Li T., Gong W. Temperature effect on the stability of 3D reinforced slopes under unsaturated flow conditions. Comput. Geotech. 2023;164:105771.

Tourchi S., Jabbarzadeh M., Sadeghi H., Lavasan A.A. Thermo-hydro-mechanical modelling of rock cliff-atmosphere interaction: the case of the Pozary test site in Czechia. EGU General Assembly 2024; 2024. Vienna, Austria. https://doi.org/10.5194/egusphere-egu24-20407.

Tourchi S., Mánica M.A., Gens A., Vaunat J., Vu M.N., Armand G. A thermomechanical model for argillaceous hard soils–weak rocks: application to THM simulation of deep excavations in claystone. Geotechnique 2023. https://doi.org/10.1680/jgeot.23.00023.

Tourchi S., Vaunat J., Gens A., Bumbieler F., Vu M.N., Armand G. A full-scale in situ heating test in Callovo-Oxfordian claystone: observations, analysis and interpretation. Comput. Geotech. 2021;133:104045.

van Genuchten M.T. A closed-form equation for predicting the hydraulic conductivity of unsaturated soils. Soil Sci. Soc. Am. J. 1980;44(5):892–8.

Varnes D.J. Landslide types and processes. Landslides Eng. Practice 1958;24:20–47.

Wang F., Konietzky H., Pang R., Zou Y., Pang B., Ismael M. Grain-based discrete element modeling of thermo-mechanical response of granite under temperature. Rock Mech. Rock Eng. 2023;56(7):5009–27.

Wang F., Pang R., Konietzky H., Hu K., He B.G., Meng D.H., Ismael M. Temperature driven real-time weakening and strengthening mechanisms of unconfined granite. Geothermics 2024;119:102973.

Wu D., Deng T., Duan W., Zhang W. A coupled thermal-hydraulic-mechanical application for assessment of slope stability. Soils Found. 2019;59(6):2220–37.

Xu X., Yue C., Xu L. Thermal damage constitutive model and brittleness index based on energy dissipation for deep rock. Mathematics 2022;10(3):410.

Zhang Y., Zhong L., Pang F., Li P., Liu F. Characteristics of energy dissipation in T-Shaped fractured rocks under different loading rates. Sustainability 2023;15(18): 13695.

Zhang Z.X., Yu J., Kou S.Q., Lindqvist P.A. Effects of high temperatures on dynamic rock fracture. Int. J. Rock Mech. Min. Sci. 2001;38(2):211–25.

Saeed Tourchi obtained his PhD degree from BarcelonaTech (UPC) and has been actively engaged in research specializing in coupled thermo-hydro-mechanical (THM) phenomena. His research interests encompass constitutive modeling of geomaterials, numerical implementation and simulation, and THM analysis of geo-energy systems. He has contributed significantly to numerous international projects, receiving prestigious funding for his work. He is currently a Postdoctoral Associate at the University of Luxembourg, focusing on the THM behavior of geomaterials and supervising Master's and PhD students. Previously, he held positions at Charles University and Aarhus University, where he led EU-funded projects addressing the impacts of climate change on landslide patterns. His extensive experience and commitment to mentoring have fostered a collaborative learning environment.